PUMP-STORAGE HYDROPOWER DESIGN IN A WASTEWATER TREATMENT FACILITY WITH AN AERATING RUNNER, ADDITIVE MANUFACTURED MATERIAL ANALYSIS, AND TESTING OF HYDROKINETIC TURBINE RUNNER.

F. M. Carter III[1] and A. Oztekin

Mechanical Engineering and Mechanics, P.C. Rossin School of Engineering and Applied Science, Lehigh University, Bethlehem, Pennsylvania 18015

ABSTRACT

The feasibility and design of a novel pumped storage system in a wastewater treatment facility is investigated. Analysis covers the added benefit of aeration, costs, and specifications. For the given sub-megawatt system, off-the-shelf runner designs are not available. This research builds on an existing pump-turbine research and design through a combination of introducing aeration into the operating processes, analysis of large format metal additive manufacturing, and testing and validation of a hydrokinetic turbine runner that uses the same response surface optimization methodology as the discussed pump-turbine design. Two concepts are generated and proposed along with a baseline scenario. Two potential site locations are provided with relevant information The Stickney Wastewater Reclamation Plant and The Navy Wastewater Treatment Plant, Joint Base Pearl Harbor-Hickam, Oahu Hawaii. Results show that aeration is the primary benefit of such a system. The system is capable of meeting the required dissolved oxygen (DO) levels in wastewater treatment. The system produces volume averaged DO levels between 1.2 and 1.4 mg/l. The system is shown to be a scalable open-loop system that can be sized for application. Area requirements of the system are acceptable due to the use of a single pedestal elevated tank The implementation timeline and nuances of this system are largely unknown. In attempt to reduce costs, advanced manufacturing methods are investigated. Investigation into advanced methods showed that mechanical properties of additive manufactured metals using a GMAW system produce equal results to wrought materials and have the potential to produce custom wear properties.

KEYWORDS

Pumped-storage; Modular Pumped-Storage Hydro; Aeration; Wastewater-treatment; additive manufacturing

[1] Corresponding Author: Electronic mail: fmc212@alum.lehigh.edu Phone: +1-631-433-2222

I. Introduction

Increasing adoption of intermittent renewable energy systems such as wind and solar is similarly increasing the demand for energy storage solutions. On a megawatt scale Pumped-Storage Hydro (PSH) is a longstanding option. PSH facilities enable greater integration of wind and solar resources into the system by reducing the curtailments of excess variable renewable generation [1]. The first pump-storage facility constructed in North America was the Rocky River (PSH) plant built in 1929 on the Housatonic river in Connecticut [2]. Many of the subsequent facilities were initially popularized by nuclear energy and developed in the time period of 1960 to 1980. As of 2015 there were a total of 40 installed PSH plants in the U.S. with a capacity of 22 GW [2]. As of 2013, PSH constituted 97% of the installed grid-scale energy storage capacity in the United States [3] and about 98% of the total energy storage capacity in the world [4]. PSH also generates additional value through its ability to aid in grid reliability [1], [5]. Reliability value additions are inclusive of frequency regulation, contingency reserves, power system stability, voltage support, and post blackout startup. As of 2015 research into the development of various grid-scale energy storage technologies, including batteries, flywheels, and compressed air energy storage was underway in the United States and internationally [6]. Developments have led to innovative research on single and adjustable speed PSH [7] and modular PSH [8],[9]. There are, however, limited options within the bounds of small and large-scale energy storage. Specifically, for pump storage this is indicative of limited off-the-shelf turbine runners and fewer commercially proven solutions. There is significant resource potential for new PSH development in the U.S., but inherent market and regulatory challenges must be overcome to realize this potential [2]. Consequently, it is necessary to produce creative, alternative energy solutions that are economically viable and environmentally friendly. One path would be to take advantage of the many thousands of miles of man-made conduits or to use wastewater to avoid environmental impacts [2]. Schleicher et al. [10] preformed a cursory hydraulic design of a modular pump-turbine runner for use in the middle-tier energy storage. This design is also suitable for deployment in micro-grid systems. The present study uses this system in combination with a water treatment facility specifically in the aeration phase.

Aeration is an increasingly popular topic due to increased attention on the environmental impact of dams and the stringent requirements and associated cost in wastewater treatment. The present study is primarily interested in aeration as it pertains to the secondary stage of treatment in wastewater facilities. Electricity use in 2004 for Wastewater Reclamation Plants (WRP) accounted for 3% of the total energy demand in the U.S. with 107 billion kWh/yr with an anticipated growth of 12% in 6 years [11]. Within the wastewater treatment process aeration is one of the largest cost centers comprising as much as 50-90% of the total energy requirements of a secondary wastewater treatment plant. Ingildsen [12] examined 11 WRP and reported an aeration energy consumption range between 24% and 90% with the overall overage of 59%. There is significant research aimed at reducing WRP energy consumption through various approaches comprising control strategies, oxygen transfer efficiency improvements, and understanding of wastewater system perturbations. In control research the use of a multi-set point dissolved oxygen on/off controller has been shown to reduce costs by 17% [13]. Further investigation using a non-linear control approach has shown promise in maintaining 2 mg/L DO

and reducing the energy used in the aeration process [14]. A different approach to saving energy is improving the oxygen transfer efficiency (OTE). Jolly et al. reported redesigned diffusers increased the standard oxygen transfer efficiency from 6%/m to 10%/m. This leads to an increased energy efficiency of 6.5 kg 0_2/kWh from 3.9 kg 0_2/kWh [15]. Finally, statistical studies of historical data on Chicago's Calumet WRP assessed high probability and lower probability perturbations and concluded that the facility is over aerating in respective events. Aeration costs could be reduced by 34% [16]. The aforementioned research takes different paths towards efficiency improvements. However, they are similar in that the aeration occurs in a power consumption phase. The current manuscript proposes several modular pump-turbine concepts that are coupled with aeration. The paradigm shift is that the wastewater aeration occurs in a power generation phase. In particular the system proposed both aerates and generates electricity.

This research uses a predesigned auto-venting solution to add additional value to the pump-turbine storage system in a water treatment application. Auto-venting methods are cost-effective and provide large airflows to turbines [17]. There are three types of auto-venting aeration methods, central aeration, peripheral aeration, and distributed aeration. The experimental study of the aeration of water through a Francis turbine was studied [18]. Different methods of air injection, both central admission at the runner cone and admission via the discharge ring were evaluated. Ultimately air admission through the cone is preferable as the location has a lower pressure than that of the discharge ring.

In this study, the combination of a m-PSH and auto-venting runner are considered in four different concepts for feasibility analysis of deployment in a wastewater reclamation plant. For the feasibility analysis two different sites have been given to provide an understanding of commercial deployment and gather realistic assumptions. The Stickney Water Reclamation Plant (SWRP) in Illinois is the largest wastewater treatment facility in the world servicing 2.3 million people in a 260 square mile area [19]. The Navy Wastewater Treatment Plant (WWTP), Joint Base Pearl Harbor-Hickam, Oahu Hawaii covers 11.61 acres, services 5.5 million gallons of wastewater per day, and accepts both domestic and industrial wastewater [20]. Each facility demonstrates bounds for such a system. SWRP located in Illinois is subject to below average commercial U.S. electricity prices of 8.77 cents/kWh. On the other hand, the Navy WWTP is exposed to above average commercial U.S. electricity prices of 26.34 cents/kWh [21]. Solar generation potential also differs between chosen locations adding another differentiator to the analysis. O'ahu, HI has a 540 watt hours/feet^2 / day potential compared to Stickney, IL which has a 400 watt hours/feet^2 / day potential[22].

The design of the pump-turbine requires knowledge of the head, flow rate, power consumption and efficiency for the unit in the pump direction. The pre-designed system shown in figure 1 has a head of 33 m, flow rate of 0.2 m^3/s, input power requirement to the shaft of 65.73 kW and upper reservoir capacity of 750,000 gallons. A response surface optimization was successfully applied in the hydraulic design. The pump hydraulic efficiency was improved by 1.06%, the turbine hydraulic efficiency was slightly affected by 0.70%. The round trip total efficiency of the system is estimated to be 78.7% [10]. The response surface optimization

method was validated in the experimental design and testing of a hydrokinetic turbine runner. The runner was tested at the Naval Surface Warfare Center, Carderock Division. After including the efficiencies of the electrical-mechanical components the mechanical power predicted vs. observed showed less than a 3% error [23].

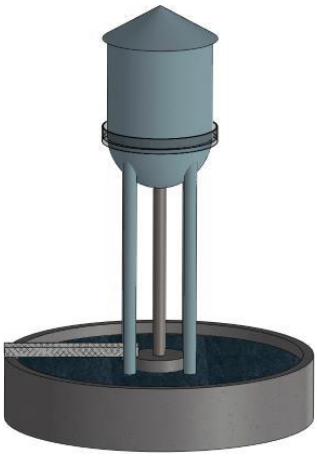

FIGURE 1. PUMPED STORAGE DESIGN (W. SCHLEICHER)

Computational fluid dynamics (CFD) simulations in both transient single phase and multiphase were performed on the pre-designed response surface optimized runner. Air admission is through the central runner cone surface during the turbine operation [26]. The mathematical modeling of oxygen dissolution was validated against prior experimental results [27]. Table 1 presents findings on the influence of bubble size, dissolution efficiency and volume averaged DO Results show that the DO in the draft tube is between 1.2 mg/l and 1.4 mg/l which is effective for wastewater treatment.

Runner Revolution		8	8.8	10.1	11	12
Dissolution efficiecny (%)	d_i = 0.1 mm	32.3	30.5	28.1	27	26.3
	d_i = 0.05 mm	36	35.3	34.7	34.7	34.3
Volume-averaged DO (mg/l)	d_i = 0.1 mm	1.23	1.2	1.24	1.28	1.32
	d_i = 0.05 mm	1.32	1.38	1.5	1.6	1.68

II. Design, Concept Generation, Modeling

Based on customer feedback and effluent treatment requirements the system has been modified to be a scalable, open-loop scheme that can integrate in a wastewater treatment plant in various ways. Figure two shows the scalable system and the open loop channels that will connect to existing second stage aeration basins, or directly to other areas of the wastewater treatment process. These gates can be programmed to control the flow of wastewater in or out of the lower reservoir.

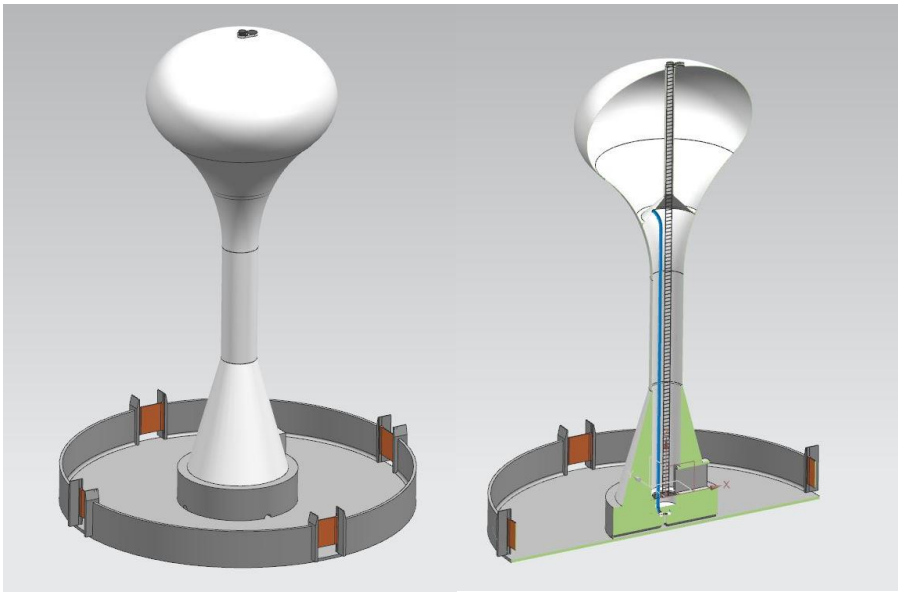

FIGURE 2. SCALABLE, OPEN-LOOP PUMPED STORAGE DESIGN

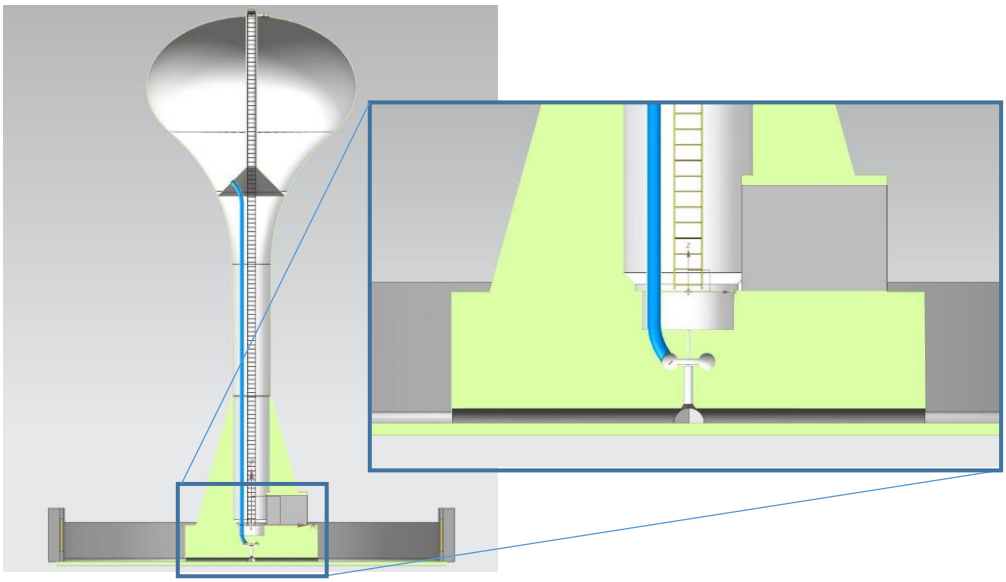

FIGURE 3. CROSS-SECTION SCHEMATIC

Figure 3 shows the cross section of the open scalable system. The upper reservoir is based on commercially available single pedestal tank with a capacity of 750,000.0 gallons [24]. Single pedestal systems require a smaller construction area and have a reduced surface area when compared to multi-column tanks [25]. In a wastewater treatment environment this would be beneficial from a reduced maintenance standpoint. Also visible is the internal ladder access to the system. This has a two-fold benefit, reduced risk of unauthorized access, and improved safety in inclement weather scenarios. The enlarged view in Figure 3 illustrates the spiral case, subfloor generation room, pump-turbine location, and draft tube. These would be modularized custom additions to the commercially available elevated tank. Also pictured in Figure 3 is the lower

reservoir. The lower reservoir is designed in a way that ingress and egress flows can be controlled, as well as accounting for a multi-unit system cases where demanded by effluent treatment requirements.

FIGURE 4. EIGHT UNIT, OPEN-LOOP PUMP STORAGE DESIGN

Figure 4 illustrates the scalable nature of the proposed system. Eight units are constructed in a 4x2 fashion. However, many arrangement scenarios are possible due to the 4 orthogonally located gates on each individual unit's lower reservoir. The total length of the system in figure 4 is 152 m, and the width is 76 m. The total upper reservoir capacity of an 8-unit system is 6 million gallons. The tabulated design specifications are given in table 2.

Combining the m-PSH system with runner aeration provides the required specifications for feasibility analysis of two concepts. Concept 1 is single modular pumped storage hydro unit with an aerating runner. Primary revenue generation on this concept will come from energy cost differentials and the offset cost of aeration. Concept 2 is also a single modular Pumped Storage Hydro unit with aerating runner. However, concept 2 also considers the potential value addition of renewable energy in particular solar. The solar input comes in the form of a 5-module array that generates 60 kW.

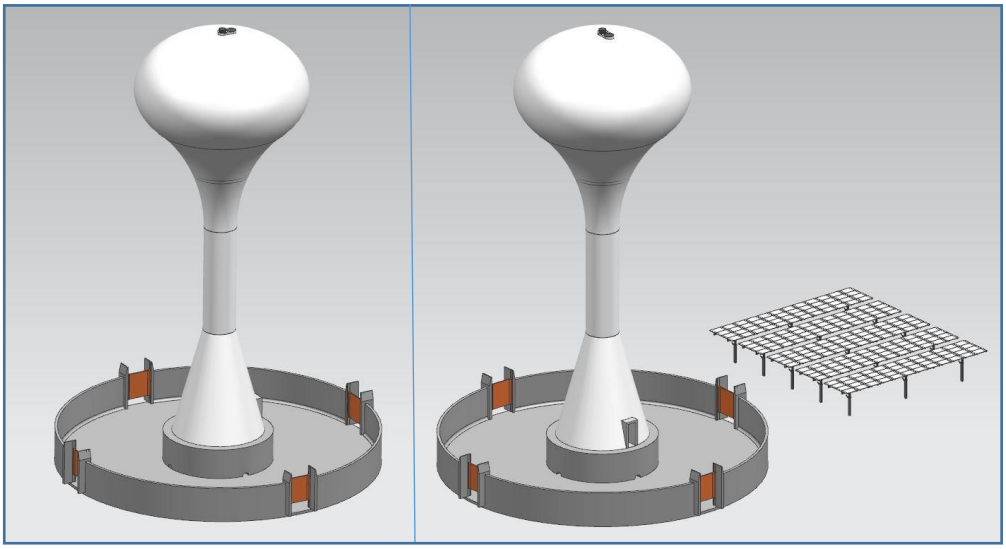

FIGURE 5. SCHEMATIC OF 4 WASTEWATER AERATING M-PSH SYSTEMS

TABLE 1: CONCEPT SPECIFICATIONS

Description	Concept 1	Concept 2
Total System Height (m)	47.6	47.6
Net Operating Head (m)	33.4	33.4
Tank Head Range (m)	12.2	12.2
Upper Tank Capacity (gallons)	750000	750000
Lower Tank Capacity (gallons)	825000	825000
Project Size (m^2)	1134.1	1134.1
Nominal Flow (m^3/s)	0.2	0.2
Total Efficiency Pump (%)	89.8%	89.8%
Total Efficiency Turbine (%)	87.6%	87.6%
Round Trip Efficiency (%)	78.7%	78.7%
Mean Generation Turbine (kW)	56.7	56.7
Mean Generation w/ Aeration (kW)	54.7	54.7
Generation (hr)	4	4
Generation Capacity (kWh)	226.8	226.8
Generation Capacity w/ Aeration (kWh)	218.8	218.8
Solar Capacity (kW)	0	60

TABLE 2: VALUES BASED ON DEPLOYMENT SITES

	Stickney WRP	Navy WWTP	Single System (U.S. Average Electrical)
Residential (cents/kWh)	12.71	29.03	13.3
Commercial (cents/kWh)	8.77	26.34	11.06
Industrial (cents/kWh)	5.98	22.58	7.21
Number of Required Systems	467	4	1
Treated Effluent Per Day (G/D)	700000000	5500000	1375000
Daily Generation from Systems (on peak)	$ 2,122,039.83	$ 54,589.97	$ 5,730.50
Daily Consumption of System (off peak)	$ 424,407.97	$ 10,917.99	$ 1,146.10
Differential	$ 1,697,631.86	$ 43,671.97	$ 4,584.40

Table 1 describes the concept specifications for the designed systems. The sole difference between concept 1 and concept 2 is that the latter adds a solar system to the generation capacity. This in commercial deployment would further offset the consumption burden of the system. Table 2 evaluates the system against two proposed locations. These locations are given as bounds. The Stickney WRP is the largest treatment facility in the world. The Navy WWTP is located in a region with some of the highest electricity costs. The values assume that there are two generation and two pumping phases daily. There is a one-hour changeover time from generation to pumping. The electricity costs are taken from published utility pricing.

TABLE 3: AERATION REQUIREMENTS

Conventional Aeration Requirements	
Activated Sludge (kWh)/million gallons	1500
Requirement per gallon	0.0015
Requirement per 750,000 gallons (kWh)	1125

Table 3 provides activated sludge aeration energy requirements. The values provided are from literature introduced in section I. Values are also provided for a single gallon of activated sludge and for the capacity of the upper reservoir of the conceptual system.

TABLE 4: SINGLE DAY AERATION

	Stickney WRP	Navy WWTP	Single System (U.S. Average Electrical)
Aeration Cost Savings	$ 19,732.50	$ 59,265.00	$ 24,885.00
Differential Generation	$ 3,635.19	$ 10,917.99	$ 4,584.40

Table 4 includes the benefit of aeration. The concept system is suitable for aerating the wastewater in the generation phase. Conventional aeration values are used to calculate the equivalent cost that would be incurred if traditional aeration would be used.

III. Conclusion

The design presented within this study shows a scalable, open-loop, modular Pumped-Storage Hydro unit with the addition of an aerating runner. CAD models and concept specifications have been provided to create a full understanding of the proposed system. Two

locations have been introduced and used to understand how such a system could be deployed. In instances such as the Stickney WRP the capital project size would exceed the footprint of the facility and would likely not be a feasible solution. However, in instances such as the Navy WWTP where only units are required and the footprint matches that of existing aeration basins the presented concepts could be feasible.

Commercial electricity costs from each location as well as a national average have been used to understand the impact of such a system. Large assumptions have been made in order to gain a preliminary understanding. The results show that the biggest financial driver for such a system would be the cost savings due to eliminating the need for traditional aeration. In bulleted form.

- Aeration has been shown to be the primary benefit of the system
- Aeration of 1.2 to 1.4 mg/l are acceptable for aerobic wastewater treatment.
- Implementation Timeline, and nuances are largely unknown and require further study
- Surface Response Optimization has been validated
- Additive manufactured material is suitable for runner material requirements.

IV. Acknowledgment

The authors would like to gratefully acknowledge that the information, data, or work presented herein was funded in part by the Office of Energy Efficiency and Renewable Energy (EERE), U.S. Department of Energy, under Award Number DE-EE0002668 and the Hydro Research Foundation.

V. Disclaimer

The information, data or work presented herein was funded in part by an agency of the United States Government. Neither the United States Government nor any agency thereof, nor any of their employees, makes and warranty, express or implied, or assumes and legal liability or responsibility for the accuracy, completeness, or usefulness of any information, apparatus, product, or process disclosed, or represents that its use would not infringe privately owned rights. Reference herein to any specific commercial product, process, or service by trade name, trademark, manufacturer, or otherwise does not necessarily constitute or imply its endorsement, recommendation or favoring by the United States Government or any agency thereof. The views and opinions of authors expressed herein do not necessarily state or reflect those of the United States Government or any agency thereof.

References

[1] V. . H. V. J. G. B. B. A. Koritarov, B. J. W. M. M. Z. Z. C. Milostan;, J. F. Y. K. T. G. G. L. B. Trouille;, P. D. K. K. E. E. B. K. I. K. and V., and Gevorgian., "Modeling and Analysis of Value of Advanced Pumped Storage Hydropower in the United States.," Argonne, IL, 2014.

[2] U.S. Department of Energy, "Hydropower VISION," 2016.

[3] M. M. Johnson, P. W. O'Connor, and R. Uria-Martinez, "2014 Hydropower Market Report," *U.S. Dep. Energy*, p. 100, 2014.

[4] S. Patel, "The Big Picture: Storage Snapshot," *Power: Business and Technology for the Global Generation Industry since 1882*, 2014. .

[5] A. Botterud, T. Levin, and V. Koratirov, "Pumped Storage Hydropower: Benefits for Grid Reliability and Integration of Variable Renewable Energy," 2014.

[6] U.S. Department of Energy, "Grid Energy Storage," 2013.

[7] V. Koritarov *et al.*, "Modeling Adjustable Speed Pumped Storage Hydro Units Employing Doubly-Fed Induction Machines," pp. 1–50, 2013.

[8] B. Hadjerioua *et al.*, *National Resource Assessment of Pumped Storage Hydropower (PSH)*. 2011.

[9] A. M. Witt, B. Hadjerioua, R. Martinez, and N. Bishop, *Evaluation of the feasibility and viability of modular pumped storage hydro (m-PSH) in the United States*, no. September. 2015.

[10] W. C. Schleicher and A. Oztekin, "Hydraulic design and optimization of a modular pump-turbine runner," *Energy Convers. Manag.*, vol. 93, pp. 388–398, 2015.

[11] K. Carns, "BRINGING ENERGY EFFICIENCY TO THE WATER AND WASTEWATER INDUSTRY: HOW DO WE GET THERE?," pp. 7650–7659.

[12] P. Ingildsen, *Realising full-scale control in wastewater treatment systems using in situ nutrient sensors*, vol. PhD. 2002.

[13] F. J. Fernández, M. C. Castro, M. A. Rodrigo, and P. Cañizares, "Reduction of aeration costs by tuning a multi-set point on/off controller: A case study," *Control Eng. Pract.*, vol. 19, no. 10, pp. 1231–1237, 2011.

[14] S. Cristea, C. de Prada, D. Sarabia, and G. Gutiérrez, "Aeration control of a wastewater treatment plant using hybrid NMPC," *Comput. Chem. Eng.*, vol. 35, no. 4, pp. 638–650, 2011.

[15] M. Jolly, S. Green, C. Wallis-Lage, and A. Buchanan, "Energy saving in activated sludge plants by the use of more efficient fine bubble diffusers," *Water Environ. J.*, vol. 24, no. 1, pp. 58–64, 2010.

[16] J. J. Zhu and P. R. Anderson, "Exploring aeration-associated energy savings at a conventional water reclamation plant," *Water Sci. Technol.*, vol. 76, no. 8, pp. 2222–2231,

2017.

[17] F. Bunea, D. M. Bucur, G. D. Ciocan, and G. Dunca, “Aeration solution of water used by hydraulic turbines to respect the environmental policies,” *EPE 2014 - Proc. 2014 Int. Conf. Expo. Electr. Power Eng.*, no. Epe, pp. 1015–1020, 2014.

[18] B. Papillon, M. Sabourin, M. Couston, and C. Deschênes, “Methods for air admission in hydroturbines,” *Cross Sect.*, 2002.

[19] W. H. Incentives, “Fact Sheet,” no. September, 2004.

[20] N. Wastewater, T. Plant, and J. B. P. Harbor-hickam, “Fact Sheet,” no. August, pp. 3–5, 2013.

[21] U. S. E. I. Administration, “State Profile and Energy Estimates,” 2017. [Online]. Available: https://www.eia.gov/state/compare/?sid=IL#?selected=US-HI-IL. [Accessed: 10-Dec-2017].

[22] Energy.gov, “Solar Energy Potential,” *National Renewal Energy Laboratory*, 2017. [Online]. Available: https://energy.gov/maps/solar-energy-potential. [Accessed: 10-Oct-2017].

[23] J. Riglin, F. Carter, N. Oblas, W. C. Schleicher, C. Daskiran, and A. Oztekin, “Experimental and numerical characterization of a full-scale portable hydrokinetic turbine prototype for river applications,” *Renew. Energy*, vol. 99, no. December, pp. 772–783, 2016.

[24] L. Phoenix Fabricators and Erectors, “Single Pedestal Water Tank Construction Specifications Tank Contractor,” 2017.

[25] L. Phoenix Fabricators and Erectors, “Single Pedestal Tanks,” 2017. [Online]. Available: http://phoenixtank.com/elevated-water-storage-productscomposite-elevated-water-tank/elevated-steel-water-tank/single-pedestal-tanks/.

[26] C. Daskiran, J. Riglin, W. C. Schleicher, and A. Oztekin, “Computational study of aeration for wastewater treatment via ventilated pump-turbine,” *Int. J. Heat Fluid Flow*, vol. 69, no. June 2017, pp. 43–54, 2018.

[27] Z. Zhou, Q. Yuan, X. Jia, W. Feng, and J. Wen, “Experimental Study and CFD Simulation of Mass Transfer Characteristics of a Gas-Induced Pulsating Flow Bubble Column,” vol. 27, no. 2, pp. 167–175, 2013.

Renewable Energy 99 (2016) 772–783

Contents lists available at ScienceDirect

Renewable Energy

journal homepage: www.elsevier.com/locate/renene

Experimental and numerical characterization of a full-scale portable hydrokinetic turbine prototype for river applications

Jacob Riglin [a], Fred Carter III [a, b], Nick Oblas [a], W. Chris Schleicher [a], Cosan Daskiran [a, c], Alparslan Oztekin [a, *]

[a] P.C. Rossin College of Engineering and Applied Science, Lehigh University, Bethlehem, PA 18015, USA
[b] Sciaky, Inc., Chicago, IL 60638, USA
[c] Turkish Military Academy, Department of Mechanical Engineering, Ankara, Turkey

ARTICLE INFO

Article history:
Received 12 April 2016
Received in revised form
2 July 2016
Accepted 25 July 2016
Available online 30 July 2016

Keywords:
Micro-hydrokinetic turbine
River applications
Turbine performance
Turbulence
Computational fluid dynamics
Experimental analyses

ABSTRACT

A preliminary hydrokinetic turbine prototype for river applications was built for experimental testing at the circulating water channel at the Naval Surface Warfare Center, Carderock Division. The prototype was designed based on numerous blade characterization and optimization analyses conducted using computational fluid dynamics (CFD) simulations. Testing was conducted for channel flow speeds ranging from 1.0 m/s to 1.7 m/s. At each tested flow speed, the generator loading was manually adjusted to produce a performance curve based off the power output from the prototype unit. In addition to manual generator loading, a solar charging unit was used to simulate turbine operation while adjoined to the ground renewable energy system (GREENS). CFD predictions were produced for the prototype using the k-ω SST turbulence model for the purpose of validation. A peak power coefficient of 0.37 was measured at a tip speed ratio of 2.50 during manual generator loading. Relative error between numerical predictions and experimental results was less than 3.0% when generator, transmission, gearbox, and other losses of selected components were applied to the numerical predictions. The solar charging converter improved prototype operation by conditioning the power output, indicating that the prototype could successfully be integrated with GREENS for portable applications.

1. Introduction

Hydropower currently yields 78 GW of energy production, per year, amounting to roughly 8% of the total electricity generating capacity of the U.S. [1]. Hydrokinetic marine current turbines (MCT) use kinetic energy from streams, rivers, and tides to drive a rotor and generate electricity. Hydrokinetic technologies are advantageous in that they require minimal civil structures for implementation compared to conventional hydropower. Current estimates for recoverable hydrokinetic energy are approximately 120 TWh/yr in United States and represent a majority of untapped hydropower resources [2]. Hydro power technology is advantageous to supply sustainable source of electricity for remote regions having water sources such as South Africa and South America. Kusakana et al. [3] performed a case study for South Africa to determine the possibility of sustainable electricity generation through hydrokinetic turbines. They compared the performance of proposed hydrokinetic turbine to other power generation systems such as wind turbine, diesel generator and standalone photovoltaic system in terms of initial capital, energy cost, total present cost and the shortage of system capacity. They concluded hydrokinetic turbine system is a better option for regions having sufficient water sources.

Hydrokinetic turbine designs developed for river application are primarily limited to low free stream velocities observed for operation and limited depth; as a result, system size and potential for deployment is restricted. Data provided by United States Geological Survey (USGS) regarding free stream velocities and average depths of rivers in the U.S and respective territories indicate that many rivers in the United States have approximately three meters or less of average depth. When considering an operational range of free stream velocities from 0.75 m/s to 2.5 m/s, approximately 51.0% of all rivers are suitable for turbine deployment [4].

Mukherji et al. [5] .and Kolekar et al. [6–8] utilized blade element momentum (BEM) theory and computational fluid

* Corresponding author.
E-mail address: alo2@lehigh.edu (A. Oztekin).

http://dx.doi.org/10.1016/j.renene.2016.07.065
0960-1481/

dynamics (CFD) analyses to optimize a horizontal axis hydrokinetic turbine rated for 12 kW. Goundar et al. [9] used a similar approach to design a marine current turbine rated for 290 kW. Performance characteristics study and structural finite element analysis of a micro hydrokinetic turbine with Archimedean spiral rotor were conducted by Riglin et al. [10] and Schleicher et al. [11]. Numerical design and characterization of a propeller-based micro hydrokinetic turbine were investigated by Schleicher et al. [12,13] and Riglin et al. [14]. Schleicher et al. [15,16] applied response surface methodology to design hydraulically efficient optimum hydrokinetic turbine. Riglin et al. [17–19] applied diffuser optimization for a micro hydrokinetic turbine and investigated the performance characteristics of two different diffuser designs having area ratio of 1.36 and 2.01.

Multiphase simulations were conducted for a micro-hydrokinetic turbine by Riglin et al. [20] to determine the performance of the unit operating close proximity to the free surface. Multiple array configurations of micro hydrokinetic turbines were studied by Riglin et al. [21] and Daskiran et al. [22] to determine the performance of adjacent units and the wake interaction influence on downstream turbine performance. The design introduced by Schleicher et al. [12,15,16] incorporated both a propeller structure and a higher value of solidity compared to observations in studies conducted with traditional hydrokinetic and marine current designs. The unit produced by Shleicher et al. [12] provided a benchmark maximum power coefficient of 0.43.

Experimental analyses of traditional designs were conducted by Kolekar et al. [8], Mycek et al. [23,24], and Bahaj et al. [25]. Performance results for two, inline units were obtained by Mycek et al. [23]and compared directly to single unit results [24]. Kolekar et al. [8] tested turbine operation in close proximity to the free surface and under increased blockage ratio for a scaled turbine model. Bahaj et al. [25] experimented on an 0.8 m diameter MCT in a towing tank allowing for power and thrust to be determined as well as the point of cavitation inception for different yaw and pitch angles.

This study highlights efforts made in producing a prototype of the non-traditional hydrokinetic turbine first introduced and optimized by Schleicher et al. [12,15,16]with characterization and prototyping efforts led by Riglin et al. [14,18–20] The main contribution of the current study is to conduct experimental analysis of a full scale hydrokinetic turbine system including runner, diffuser, nacelle and ellipsoid supports. The prior characterization and optimization numerical studies of the present authors were conducted without the presence of nacelle, ellipsoid supports and even diffuser for some of them. Experimental results were used to validate numerical predictions of an identical system operating under similar loading.

The present study of propeller-based hydrokinetic turbine differs from aforementioned experimental studies of traditional hydrokinetic turbines through its some features. Firstly, a diffuser was augmented to the turbine runner to enhance the system performance. The prototype is modelled and designed to be compact and easily person-portable. The developed hydrokinetic turbine system can simply be transported and installed in streaming water to generate power in a short time. The system was designed to integrate into the Ground Renewable Energy System (GREENS) allowing for tandem hydropower and solar power generation. Similar efforts have been made, including by Li et al. [26], to integrate solar and hydro energy conversion into a single system. The present body of work highlights both characterization of the hydrokinetic prototype through simple electrical loading as well as the implementation of a solar charging converter to mimic GREENS implementation. Testing was conducted at the circulating water channel (CWC) at the Naval Surface Warfare Center, Carderock Division. Results from both tests are used to validate pre-existing numerical predictions used in design, characterization, and optimization.

2. Prototype design

2.1. Blade design

The blade design incorporated in the prototype was originally generated by Schleicher et al. [12] using predetermined goals for output power, set operating conditions, and an empirical relationship of lift and drag for cascading flat plates generated by Cebrián et al. [27]. The final blade and diffuser geometries were optimized by Schleicher et al. [15,16] using rapid CFD processes and central composite design methodology. For the optimization of the final design, a full factorial experiment was conducted for a free stream velocity of 1.5 m/s. The flow speed was selected such that the turbine would be operable over the broadest range of applicable conditions for useful power generation as indicated by river data. Equations for blade generation, including blade angles, chord length, and wrap angle are included in [12].

For the actual prototype design, Schleicher [16] incorporated a B-spline in the rapid CFD optimization implemented allowing for blade curvature to improve predicted power and thrust outputs. The final propeller based blade design is shown in Fig. 1 with the wrap angle ($\Delta\theta$), blade angle (β'), relative flow angle (β) to the turbine's rotating frame of reference, and meridional length (Δm) listed. The optimized B-spline to produce the curvature in the blade is shown in Fig. 2. This curvature leads to corresponding blade angle from the leading edge (LE) to the trailing edge (TE). The runner design observed Fig. 1 was augmented with a diffuser with an area ratio (AR) of 1.31. The values of diffuser length (L) and diffuser angle (θ) for the implemented part were 0.381 m and 12°, respectively. The full list of turbine and diffuser design parameters incorporated in the final design are provided in Table 1.

The full turbine-prototype design is detailed below in Fig. 3 with assembled nacelle, hub, elliptical supports, blades, and diffuser geometries. The inlet of the overall system can be observed in Fig. 3a. The role of the diffuser and leading cone expand beyond improved performance and in the present design serve as the primary structural supports of the overall system. The diffuser is the primary component of the entire unit design. The nacelle has a slightly larger diameter and allows for the back end elliptical supports to be fixed perpendicular to the diffuser.

2.2. Mechanical-electrical power conversion

Based on the optimization work done by Schleicher, the design had a predicted output of approximately 431.4 W of mechanical power at a free stream velocity of 1.5 m/s. A 20 A, continuous DC permanent magnet generator produced by Windstream LLC was selected for mechanical-to-electrical power conversion. Utilizing a DC generator over AC options allowed for a broader range of flexibility for future GREENS interfacing. The generator output specifications along with the anticipated primary operating point at which the prototype is designed for is provided in Fig. 4. Under the present designed conditions, a 48 V DC output with a current of approximately 8 A would be observed under flow conditions of 1.5 m/s and a blade rotation rate of 115 RPM. The selected generator may only operate continuously at currents less than 10 A with a cut-off at 20 A. Due to the present limitations on the selected generator, operational free stream velocity is limited to roughly 1.9 m/s.

The rotation rate of the optimized turbine blade under ideal loading is 115 RPM. According to the operation point located in Fig. 4 the rotation rate of the generator shaft is approximately 1150

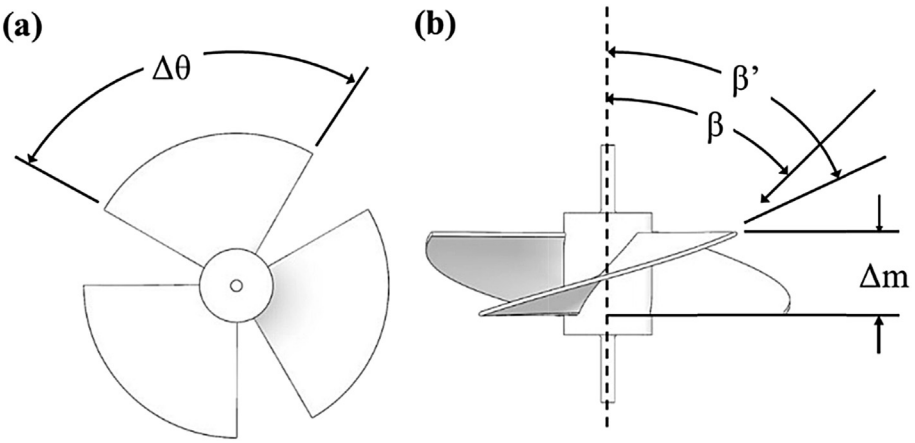

Fig. 1. Optimized propeller turbine runner (a) front view and (b) top view.

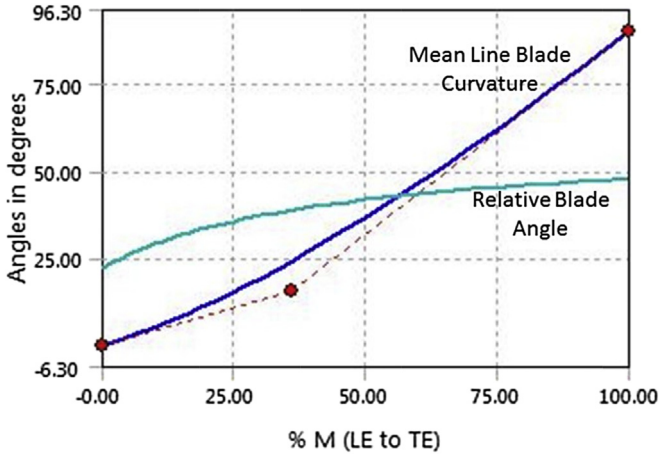

Fig. 2. Mean line blade curvature from the leading edge (LE) to trailing edge (TE) and relative blade angle (teal line) for prototype blade geometry.

Table 1
Geometric parameters for blade curvature and diffuser [16].

Variable	Value	Variable	Value
D_t (tip diameter)	0.6826 m	D_{In} (diffuser inlet diameter)	0.6985 m
D_h (hub diameter)	0.1651 m	D_{Out} (diffuser outlet diameter)	0.8001 m
Δθ (wrap angle)	90.0°	L (diffuser length)	0.381 m
β (relative flow angle)	62.0°	Z_B (blade number)	3
β' (blade angle)	76.3°	θ (diffuser angle)	12.0°
Δm (meridional length)	0.1524 m	AR (diffuser area ratio)	1.31
σ (solidity)	0.83		

RPM.

Therefore, an in-line gearbox with a 10:1 ratio was selected to couple the turbine shaft and the generator shaft. A PE-W Series gearbox and custom mount were selected from GAM to attach directly onto the generator. Torque produced by the turbine was predicted from the optimization results to be 35.83 N-m. After the 10:1 step-down in torque, the result still exceeds the 0.153 N-m of startup torque required for the generator. A male-male elastomer coupling was selected to dampen any possible shaft vibration and slight misalignments existing between the turbine runner shaft and the gear box after assembly.

The input voltage range of GREENS is 18–32 V DC at a maximum power of 1.0 kW. Due to the input voltage limitations of the system, a DC/DC converter was selected to enable suitable conversion to within the acceptable input range. The converter used for experimentation is a solar charging converter that mimics the conversion that would be observed in GREENS operation. Efficiencies of each component are contained in Table 2. The efficiency of the generator is approximately 0.96 near the optimum, design operating conditions with the value dropping to around 0.90 as generator operation deviating from the selected design point. The subassembly of the generator is provided below in Fig. 5.

2.3. Rigging and supports

The prototype was comprised of components fabricated using both 316/304 stainless steel and 6061* aluminum alloys. The diffuser supports shown in Fig. 3 have an elliptical cross section with major and minor axes of 0.0254 m and 0.0508 m. Supports were selected based on predicted force exerted by flowing water on the components of the system at expected testing conditions. The equation for velocity magnitude, $|U|$, is provided below:

$$|U| = \sqrt{U_\infty^2 + \left(\frac{\Omega D}{2}\right)^2} \tag{1}$$

Using Eq. (1), the distributed load on each support is estimated to be $F_D = 67.88$ N. The force exerted on the beam is negligible when considering the structural integrity of the supports. The velocity magnitude used far exceeds the flow speed of the oncoming flow that will be experienced by the supports. The analysis provides an estimate of thrust that would be generated by the ellipsoid supports and ensures that the tubing will be able to withstand the anticipated dynamic loading and remain structurally sound.

In order to enable testing, it was necessary to create a mounting structure. Stainless-steel box tubing was joined with the nacelle tube core. The box tube is 4 inches by 2 inches by 1/8 inch thick. This section was drilled and arc welded onto the nacelle. The tube was welded onto to core of the nacelle using 0.899 mm diameter stainless steel filler wire, a tri-mix shielding gas comprised of argon, helium, and $C0_2$, and constant voltage welding parameters. This tube allows for the device to be rigidly secured by inserting and bolting it onto a support beam. In addition to the tubing adjoined to the nacelle, the ellipsoid supports were welded onto the front cone and the nacelle using the same gas metal arc welding (GMAW) procedure. A gas tungsten arc welding (GTAW) was used to ensure a more precise watertight fit at the end of the nacelle. A watertight pass through gasket is mounted on the back cap of the

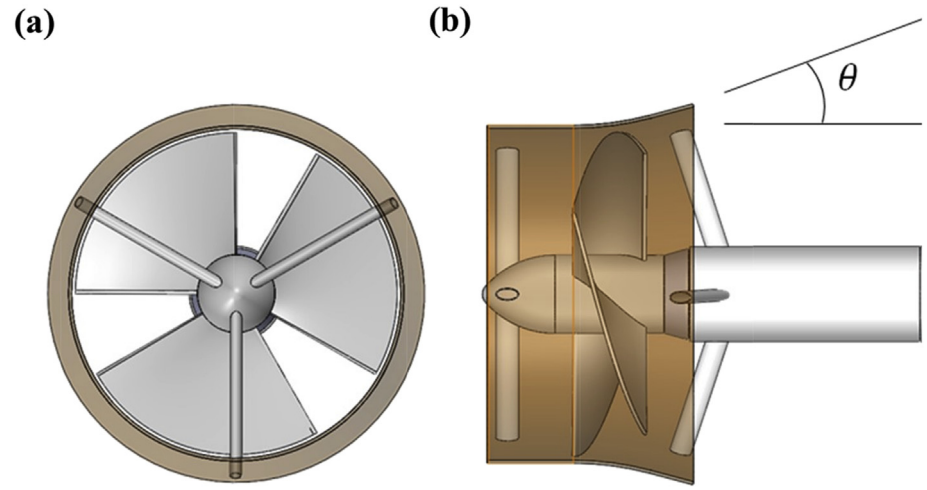

Fig. 3. Prototype design (a) front view and (b) side view from Schleicher et al. [14,19].

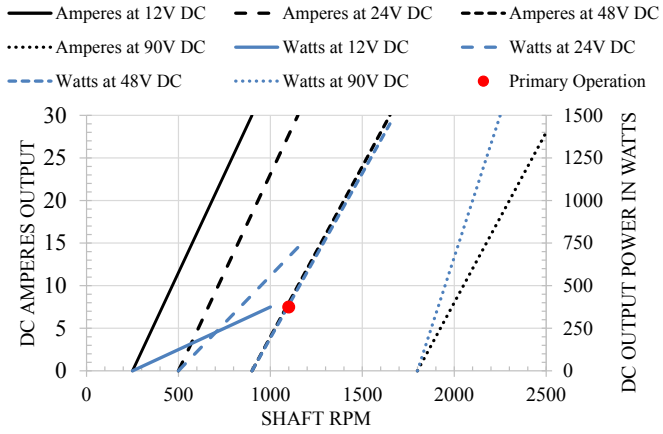

Fig. 4. Shaft RPM vs DC output for chosen generator.

power monitoring system, the generator output, and various process monitoring.

For mooring purposes, a mild steel beam was constructed of two square 38.1 mm, 6.31 mm thick steel beams. The individual beams were welded together using a GMAW system creating a more rigid beam to resist bending and torsion caused by turbine generated thrust during operation. The beam is over 1.8288 m long. The final, assembled prototype unit is shown below in Fig. 6.

3. Numerical modeling

3.1. Meshing

In numerical optimization process of hydrokinetic turbine [15], the turbine domain was discretized with coarser mesh to reduce the total computational time for 135 simulations. Due to the error involved with mentioned rapid-CFD method, it was necessary to

Table 2
Prototype component efficiencies [14].

Efficiency	Generator	Gear box	DC/DC converter	Transmission losses-wiring
η	0.96	0.94	>0.85	0.97

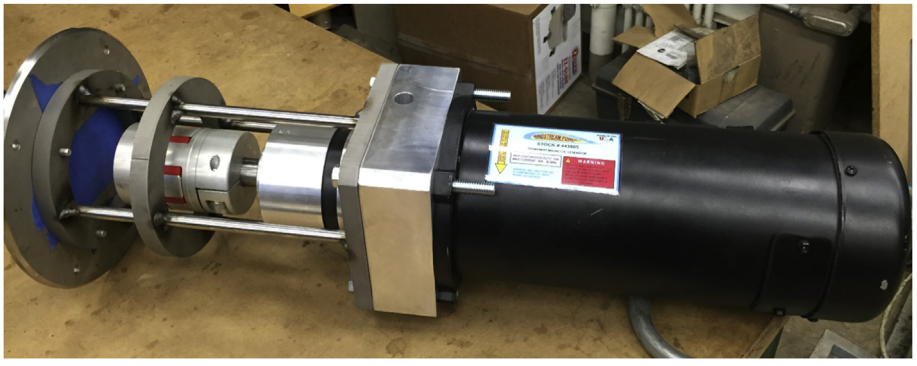

Fig. 5. Generator subassembly.

nacelle allowing for clear tubing to feed multiple electrical wires from the generator to the load cell. These wires are used for the

conduct more refined simulations. In previous work conducted on the propeller-based turbine design, optimization, and

Fig. 6. Entire prototype assembly.

characterization by Riglin et al. [14,18–20]and Schleicher et al. [12,15,16], structured, hexahedral cells were used exclusively for grid generation. In the present body of work, due to the complexity involving the diffuser-support design, a hybrid mesh was required to accurately model the prototype system. A cylindrical domain with dimensions consisting of $14.0D_t$ in diameter and $20.0D_t$ in length was used to generate predictive results of unit operation.

A full scale model was analyzed without the presence of the support beam or the support fixture welded onto the nacelle. The overall assembly placed in the computational domain involves turbine rotor, ellipsoid supports, nacelle and diffuser as depicted in Fig. 7. Three separate subdomains were used: the river domain, the diffuser-support domain, and the turbine runner domain. Hexahedral cells were used for the river domain and turbine runner domain with unstructured tetrahedral and wedge cells were used within the diffuser domain. A total of 25.14 million cells were used with approximately 7.17 million of which were allotted to capturing the flow physics within the runner subdomain. The leading edge of the prototype blades were positioned $5.0D_t$ from the inlet of the computational domain.

Fig. 8 contains the surface grid applied to a single runner blade within the runner subdomain. The resolution of the grid along the tip of the blade is observed in Fig. 8b. Within Fig. 8a and b, for the side and front view of the surface meshing, emphasis was placed on resolving the tip of the blade, the leading and trailing edges, and the location of blade curvature resulting from the B-Spline applied in Fig. 2. The grid utilized in the present body of work resulted in average y^+ values ranging between 25.0 and 50.0 along the walls of the turbine blades and hub, ensuring that flow separation is being

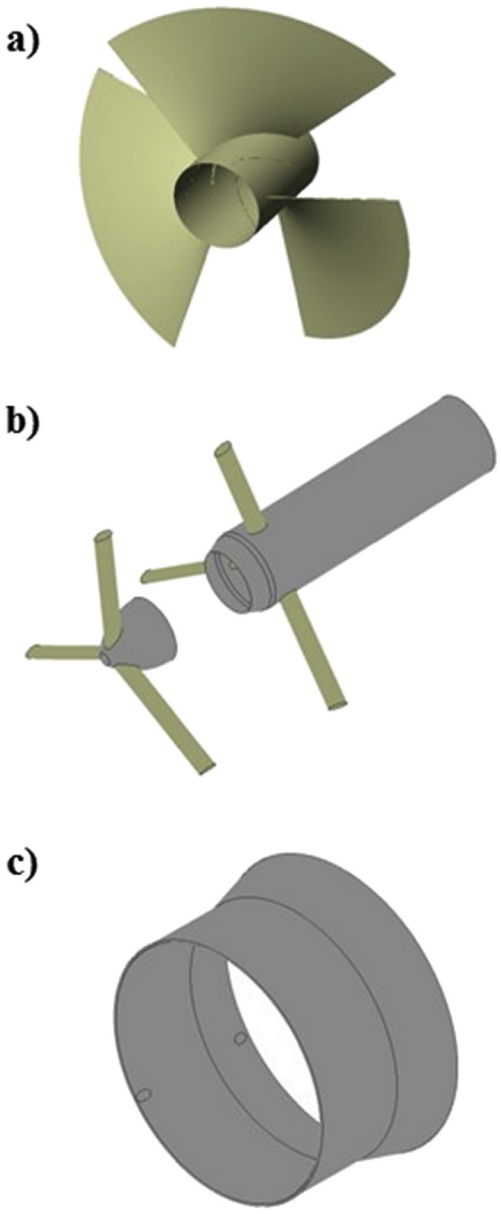

Fig. 7. Components included in the computational domain: a) turbine rotor, b) ellipsoid supports and nacelle, c) diffuser.

accurately captured. For the turbulence model utilized, y^+ values of ranging from 25.0 to 100.0 are acceptable for accurate results.

3.2. Turbulence and flow modeling

The flow field near the turbine within the river can be characterized using the Reynolds number, provided below:

$$Re = \frac{\rho U_\infty D}{\mu} \tag{2}$$

Here Re is the Reynolds number, D is the diameter, ρ is the fluid density, U_∞ is the free stream velocity magnitude, and μ is the dynamic viscosity. All simulations were conducted for a Reynolds number of ~14.33×10^6 based on the diameter of the cylinder defining outer boundary of the computational domain (the channel diameter) and ~1.02×10^6 based on the tip diameter.

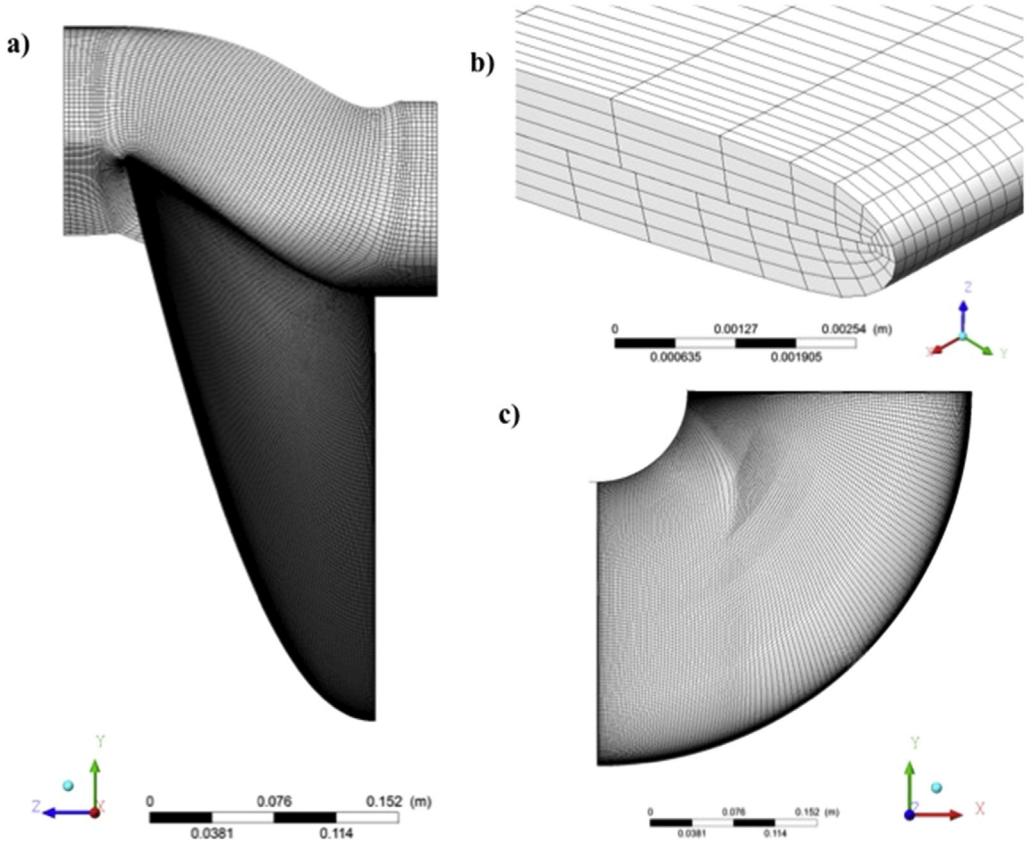

Fig. 8. (a) Side view, (b) blade tip, and (c) front view of the surface structure along the turbine blade surface.

The computations were carried out using ANSYS FLUENT. Steady-state simulations with multiple reference frames were conducted for each case using a pseudo-transient, coupled pressure-velocity solver. A rotating reference frame was applied within the turbine runner domain, which transformed flow from an unsteady inertial frame to a steady non-inertial frame with the inclusion of the centrifugal and Coriolis forces into the transport equations.

$$\frac{\partial U_{r,i}}{\partial x_i} = 0 \tag{3}$$

$$\frac{\partial U_{r,i}}{\partial t} + U_{r,j}\frac{\partial U_{r,i}}{\partial x_j} = -\frac{1}{\rho}\frac{\partial p}{\partial x_i} - 2\varepsilon_{ilq}\Omega_l U_{r,q} - \varepsilon_{ilq}\varepsilon_{qsw}\Omega_l\Omega_s x_w + \nu\frac{\partial^2 U_{r,i}}{\partial x_l \partial x_l} \tag{4}$$

where U_r is the velocity relative to the rotating reference frame. The spatial coordinate is represented by x and time by t. Static pressure is depicted by p, density by ρ, angular rotation rate of the blade by Ω, ε is the permutation symbol and the subscripts i, j, l, q, s, and w are index placeholders. Through the use of the pseudo-transient solver, time steps with arbitrary values were used iteratively as the solution progressed to what could be considered steady-state.

Turbulent flow characteristics were modeled using Menter's k-ω Shear Stress Transport (k-ω SST) [28,29] two-equation eddy-viscosity model. This model offers improved prediction of adverse pressure gradients in the near wall region compared to the standard k-ω and k-ε models. The model utilizes Bradshaw's observation that within the boundary layer wake region the turbulent shear stress is proportional to the turbulent kinetic energy [30]. The k-ω SST model mimics the k-ω model in near wall regions which allows for flow separation to be more accurately predicted. At regions distant from wall boundaries, the k-ω SST model transitions to k-ε model-like behavior, and is more suitable for modeling wakes, free-shear effects, and recirculation. The k-ω SST model utilizes the strengths of the k-ω model and the k-ε model ensuring that both the turbine performance characteristics and wake profiles produced are accurate. The equations for kinematic eddy viscosity, turbulent kinetic energy, and specific dissipation rate are:

$$\nu_T = \frac{\alpha_1 k}{\max(\alpha_1\omega, SF_2)} \tag{5}$$

$$\frac{\partial k}{\partial t} + U_j\frac{\partial k}{\partial x_j} = \tau_{ij}\frac{\partial U_i}{\partial x_j} - \beta^* k\omega + \frac{\partial}{\partial x_j}\left[(\nu + \sigma_k\nu_T)\frac{\partial k}{\partial x_j}\right] \tag{6}$$

$$\frac{\partial \omega}{\partial t} + U_j\frac{\partial \omega}{\partial x_j} = \alpha S^2 - \beta\omega^2 + \frac{\partial}{\partial x_j}\left[(\nu + \sigma_\omega\nu_T)\frac{\partial \omega}{\partial x_j}\right] + 2(1 - F_1)\sigma_{\omega 2}\frac{1}{\omega}\frac{\partial k}{\partial x_j}\frac{\partial \omega}{\partial x_j} \tag{7}$$

where ν_T is the turbulent eddy viscosity, ν is the kinematic viscosity, k is the turbulent kinetic energy, ω is the specific dissipation rate, α_1 is a closure coefficient, S is the mean rate-of-strain tensor, and F_1 and F_2 are blending functions. More details on the k-ω SST turbulence model, other k-ω model variations, and the specific blending function formulas are documented in greater detail by Wilcox [30].

Pressure corrections were produced through the use of the Pressure Staggering Option (PRESTO!) scheme. Momentum,

turbulent kinetic energy, and turbulent dissipation rate were all modelled with second-order upwind schemes. A uniform velocity inlet condition was applied to the inlet with a constant 1.5 m/s free stream fluid speed to parallel the design conditions used to develop the blade-diffuser setup. The outlet was set to a constant gauge pressure of 0 Pa with a zero-gradient velocity. The channel hydraulic diameter, D, and the turbulent intensity were applied as the turbulent boundary conditions at the inlet and outlet. The turbulent intensity used is as follows:

$$I = 0.16(Re_D)^{-1/8} \times 100\% \tag{8}$$

Here I is the turbulent intensity and Re_D is the Reynolds number based on the hydraulic diameter. The convergence criteria for momentum, continuity, and turbulence parameters of relative residuals were set to 10^{-4}. For fully turbulent inlet boundary conditions present with a flow velocity of 1.5 m/s, a turbulent intensity of approximately 3% was experienced. This turbulence intensity falls under idealized flow within a river with turbulence capable of approaching 15%. Mycek et al. [24] shows experimental results under both turbulence conditions.

3.3. Preliminary numerical predictions

Performance of the prototype was characterized using the following terms:

$$\lambda = \frac{D_t \Omega}{2U_\infty} \tag{9}$$

$$C_P = \frac{\dot{W}}{\frac{\pi}{8}\rho U_\infty^3 D_t^2} \tag{10}$$

$$C_T = \frac{T}{\frac{\pi}{8}\rho U_\infty^2 D_t^2} \tag{11}$$

Here λ is the tip speed ratio and represents the ratio between azimuthal speed at the blade tip and the free stream speed. The angular velocity of the turbine blade is represented by Ω. Values of power and thrust are characterized by $\dot{W}$ and T. Power coefficient and thrust coefficient are given as C_P and C_T. Applying Eq. (9) through (11) to the predicted power and thrust resulting from steady state simulations were normalized and plotted in Figs. 9 and 10. Fig. 9 shows the power coefficient as a function of tip speed ratio. The curve observed only represents mechanical power of the prototype without the influence of any electrical-mechanical losses. Peak performance of the unit is predicted to be at the tip speed ratio corresponding to the design point of the blades. The primary numerical simulations of hydrokinetic turbine system [14] were conducted without the presence of ellipsoid supports and predicted power coefficient value of 0.68 at the best efficiency point. The peak power coefficient predicted at 0.50 for the present study shows a significant drop from power predictions without the presence of supports [14]. The thrust coefficient for both the overall prototype and each set of structural components are highlighted in Fig. 10. The turbine blades result in the most generated thrust with the supports consistently providing thrust coefficient value of approximately 0.05. Fig. 10indicates that the thrust of the current prototype, even with supports, is less than that predicted by Riglin et al. [18] for a preliminary two blade design, despite a larger overall system.

3.4. General mesh study

Schleicher et al. [12] verified discretization convergence for

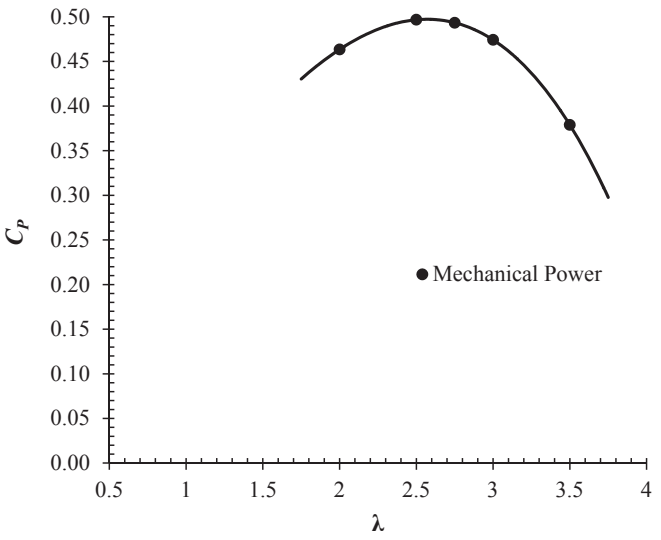

Fig. 9. Prototype power coefficient predictions as a function of tip speed ratio.

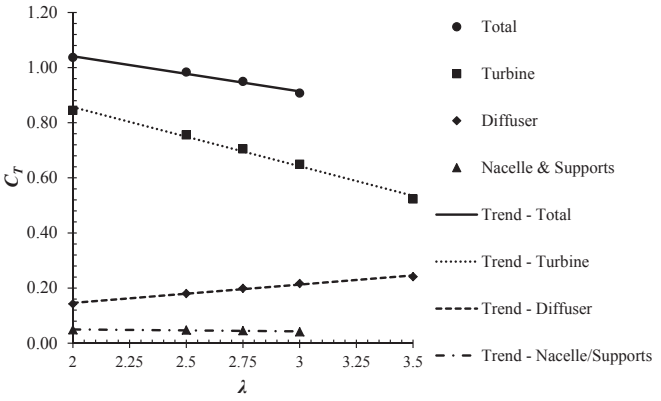

Fig. 10. Prototype thrust coefficient predictions as a function of tip speed ratio.

propeller-based turbine designs in steady state simulations. Richardson extrapolation based Grid Convergence Index (GCI) method outlined by Roache [31–33] and Celik et al. [34] were used to quantify the error band on the generated solution due to discretization error. For a two-blade design, Schleicher et al. used three separate meshes containing 1.2×10^6 cells, 5.9×10^6 cells, and 14.6×10^6 cells. From the extrapolations, it was determined that the 5.9×10^6 cell mesh had a discretization error of only 3.1% for the resulting power and 2.0% for the resulting thrust. According to this study, it is estimated that roughly 2.25 million cells per blade region are required to adequately produce accurate turbine performance results. The present three blade design has roughly 1 million more cells confined within a region approximately 0.25 the size of the turbine domain used by Schleicher, indicating that a higher level of accuracy is expected. Turbine runner subdomain was mapped using ANSYS TurboGrid which produces high-quality hexahedral cells with smooth transition between elements near blade region. The mesh quality parameters for turbine subdomain in the present study was obtained as follows: the face angle is altering between 29.1° and 152.5° which is suggested to be in the range of 18° and 165° as default, the maximum element volume ratio which is used to obtain element expansion rate is 8.28 and the maximum edge length ratio is 123.4. The high edge length ratio was performed in near-wall region to resolve the boundary layer

accurately.

4. Experimentation

4.1. Experimental setup

The CWC has a working cross-section for testing of 6.7056 m wide and up to 2.7432 m in depth. The length of the testing region of the channel is 18.288 m. Two movable bridges are able to locate along the length of the test section region. There is approximately 1.5 m of clearance between the free surface level and the rigging portion of the bridge when the channel is filled to maximum capacity. The channel may maintain flow speeds up to 5.2 m/s [35]. The blockage ratio between swept area of the turbine to the channel cross sectional area is 0.020, indicating that operation of the turbine can be considered free stream with no influence of wall and shear boundaries. The developed prototype was positioned such that it was centred within the channel at a depth of 1.3716 m below the free surface level. The designed support beam rigidly anchored the prototype to the bridge using a custom made mounting plate. Clear tubing containing electrical wiring was wrapped and tied down to the support beam while being led to the electrical system.

Two separate experimental tests were conducted. First, the generator was connected directly to an electronic load generator allowing the user to manually adjust the load on the prototype while in operation. A solar charging converter (SCC) was introduced for the second test setup. The electrical circuit that produced the second set of testing results is detailed below in Fig. 11. In Fig. 11, five primary components of the electrical analysis are included: Generator, Capacitor, SCC, Battery Bank, and the Electronic Load. The battery bank and SCC mimic the GREENS system in allow for input power by the prototype to be controlled and stored until power is drawn. Voltage and current are represented by V and I, respectively, with capacitance represented by C.

4.2. Procedure

Though two separate experimental tests were conducted, the turbine was under hydraulic loading for a continuous, 2.5-h period of time during which all data was recorded. Data was logged at a sampling rate of 1 sample per second. Results were recorded over a range of channel flow speeds ranging from 1.0 m/s to 1.7 m/s. Initially, the channel velocity was slowly increased to determine the start-up flow speed required to initiate the rotation of the prototype runner. After the start-up flow speed was determined, the order of channel flow speeds tested was as follows: {1.6 m/s, 1.5 m/s, 1.4 m/s, 1.2 m/s, 1.0 m/s, 1.6 m/s, 1.7 m/s, 1.5 m/s}. The final flow speed investigated, 1.5 m/s, was conducted with the SCC unit incorporated while the rest utilized manual generator loading. At each flow speed, constant electronic loading amperage, I_L, was applied to the generator with the voltage being measured as a function of time over a 2-min period. The amperage was adjusted in roughly 2 A increments between 0 A and 12 A to capture the entire power output capability of the prototype.

4.3. Uncertainty analysis

Uncertainty in the power production and tip speed ratio of the prototype was quantified using empirical relationships produced from the generator specifications shown in Fig. 4. Using the empirical relationships was necessary to determine the rotation rate of the prototype runner, thus allowing for the formulation of tip speed ratio as shown in Eq. (9). In Eq. (12), the resulting power after all losses is determined from the measured amperage and voltage of the electronic load. From Fig. 4, it is known that for a constant voltage, there is a linear relationship between output current and shaft rotation rate of the generator. Expanding on this linear relationship, empirical relationships were formed for the slope and intercept based upon the output generator voltage, as shown below:

$$\dot{W} = I_L V_L = I_G V_G \eta_{wire} \tag{12}$$

$$I_G = m_I \Omega_G + b_I \tag{13}$$

$$m_I = 0.0657 V_G^{-0.11} \tag{14}$$

$$b_I = -0.7523 V_G - 3.6801 \tag{15}$$

where I_L is the current measured by the electronic load, V_L is the voltage measured by the electronic load, I_G is the current measured at the generator, and η_{wire} is the efficiency in transmission through the wires. For the empirical formulas: m_I is the slope of the generator current, b_I is the intercept of the generator current, and Ω_G is the rotation rate of the generator shaft. Eqs. (14) and (15) had R^2 values exceeding 0.995 indicating strong agreement between the relations and the specifications provided.

Substituting Eqs (13) through (15) into Eq. (12) result in a final equation of power as a function of generator voltage and transmission efficiency. Rearranging Eq. (16) results in a formulation for the generator rotation rate, shown in Eq. (17).

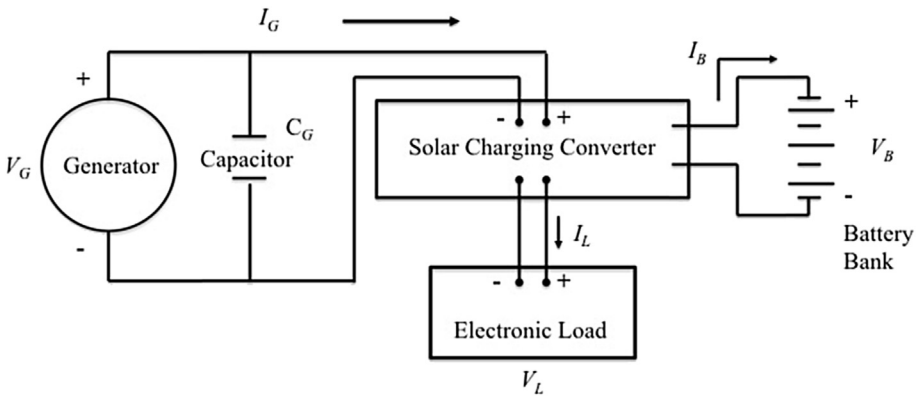

Fig. 11. Electrical schematic for the second test setup conducted with the solar charging converter.

$$\dot{W} = \left(0.0657V_G^{0.89}\Omega_G - 0.7523V_G^2 - 3.6801V_G\right)\eta_{wire} \tag{16}$$

$$\Omega_G = \frac{\left(\frac{\dot{W}}{\eta_{wire}}\right) + 0.7523V_G^2 + 3.6801V_G}{0.0657V_G^{0.89}} \tag{17}$$

Eq. (18), shown below, highlights the relationship between prototype runner rotation and generator shaft rotation based upon gear box selection. Eqs. (17) and (18) were applied to Eq. (9) to produce a final relationship of tip speed ratio for experimental results, shown in Eq. (19) below:

$$\Omega = \frac{\Omega_G}{r} \tag{18}$$

$$\lambda = \frac{D_t}{2U_\infty r}\frac{\left(\frac{\dot{W}}{\eta_{wire}}\right) + 0.7523V_G^2 + 3.6801V_G}{0.0657V_G^{0.89}} \tag{19}$$

where r is the gear ratio of the selected gear box for mechanical-mechanical power conversion which is a constant of 10 for the present study.

Uncertainty in the power results obtained was determined directly by averaging the power coefficient produced based on the current and voltage measured and finding the deviation from the average over a 25 s interval. Equations for average power coefficient and standard deviation of the power coefficient are provided below:

$$\overline{C_P} = \frac{I_L}{\frac{\pi}{8}\rho U_\infty^3 D_t^2}\int_{t_o}^{t_f} V_L dt \tag{20}$$

$$\sigma_{C_P} = \sqrt{\frac{1}{N}\sum_{i=1}^{N}\left(C_{P,i} - \overline{C_P}\right)^2} \tag{21}$$

Here $\overline{C_P}$ is the average power coefficient, t_o is the initial time, t_f is the final time, N is the number of data points incurred over the 25 s interval, and σ_{C_P} is the standard deviation in power observed.

The final standard deviations expected in the tip speed ratio were produced in terms of deviation of the prototype runner rotation rate, deviation in blade tip diameter resulting from the manufacturing processes, and the differentiated terms from Eq. (19). Standard deviation of the tip speed ratio is highlighted in Eq. (23). Results obtained by Eqs. (19) and (23) hold for values of voltage greater than approximately 10–12 V but break down as voltage diminishes due to the nature of the empirical relationship in Eq. (14).

$$\sigma_\Omega = \frac{1}{m_l V_G r}\sigma_{C_P} \tag{22}$$

$$\sigma_\lambda = \sqrt{\left(\frac{\partial\lambda}{\partial\Omega}\right)^2\sigma_\Omega^2 + \left(\frac{\partial\lambda}{\partial D_t}\right)^2\sigma_{D_t}^2} \tag{23}$$

5. Results

5.1. Performance characteristics

Measured power recorded during testing along with corresponding levels of error associated with the time-averaged power and tip speed ratio formulation are included in Fig. 11 for the fluid speed of 1.5 m/s, 1.6 m/s and 1.7 m/s. The presented measured results were obtained using through applying an electrical load to the generator at specified channel flow speeds. Through varying the electrical loading, the rotation rate of the runner was altered allowing for prototype efficiencies to be obtained over a wide range of applicable operating conditions. Measured results obtained from the data acquisition system were averaged over a 30 s time period at each testing condition to produce the average power coefficient results displayed. Fig. 12a displays the power coefficient measured at an operational channel flow speed of 1.5 m/s. The peak resulting efficiency for a flow speed of 1.5 m/s was approximately 0.35. Fig. 12b and c shows that at slightly higher operating channel flow speeds, the peak power coefficient of the prototype increases to roughly 0.37. In all cases, the same operational range of tip speed ratios are between roughly 1.0 and 3.75. Due to the nature of the equations used for interpolating the rotation rate of the turbine, confidence exists in results for tip speed ratios only for values of 1.50 and above. Fig. 13 contains the power observed for channel flow speeds of 1.0 m/s, 1.2 m/s, and 1.4 m/s. The data included highlights how the peak efficiency point is reduced as the flow

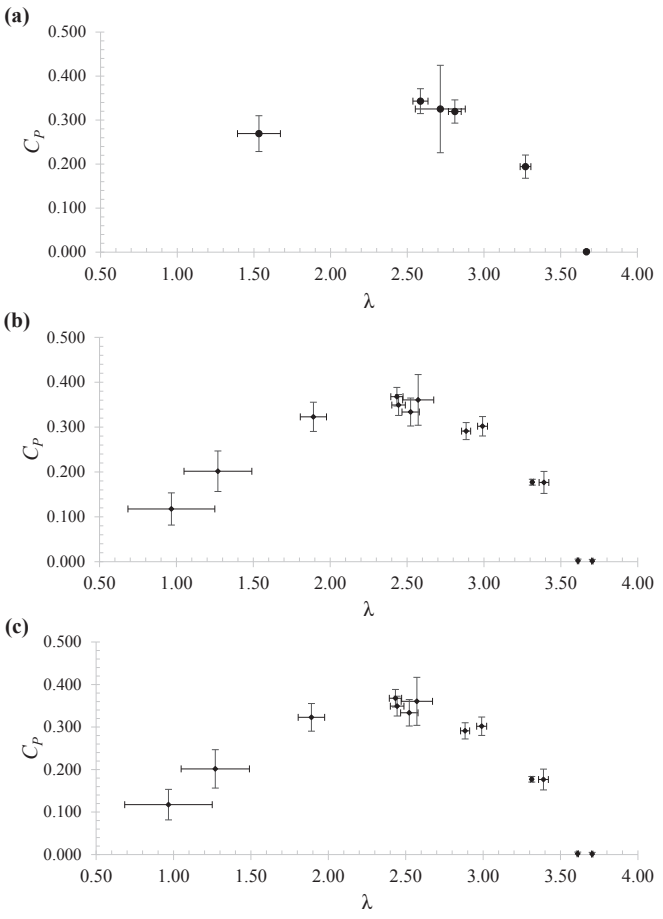

Fig. 12. Measured power coefficient as a function of tip speed ratio at a channel flow speed of a) 1.5 m/s, b) 1.6 m/s, and c) 1.7 m/s.

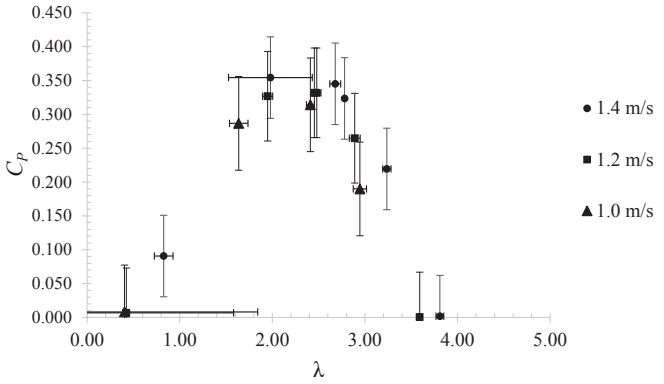

Fig. 13. Measured power coefficient as a function of tip speed ratio at a channel flow speeds varying between 1.0 m/s and 1.4 m/s.

speed diminishes in magnitude. At 1.4 m/s, peak efficiency of approximately 0.36 is maintained with little contrast to that of the data obtained at flows of 1.5 m/s and above. However, flow speeds of 1.2 m/s and 1.0 m/s the peak performance subsides to values of approximately 0.33 and 0.30. The reduction observed is primarily due to the disparity between operating conditions and the conditions for which the device was designed for. Additionally, flow dynamics at a lower angular velocity result in less separation along the blades which, in the present design, are highly dependent upon pressure difference between upstream and downstream sides. Traditional units operate at higher ranges of optimum tip speed ratio ranging from 3.5 to as high as 6.0 resulting in a higher blade rotation rate under identical flow conditions.

Eq. (24) is used to provide a final overall system efficiency for expected operation. Numerical mechanical power predictions generated from CFD analyses in Fig. 9 were subjugated to the values of efficiency for the prototype contained in Table 2 using Eq. (24), shown below:

$$C_{P,overall} = C_P \eta_{SCC} \eta_G \eta_{gear} \eta_{wire} \tag{24}$$

Here η_{SCC} is the efficiency of the DC/DC SCC, η_G is the efficiency of the generator, and η_{gear} is the efficiency of the gear box.

Fig. 14 contains time averaged power results produced from the manual generator loading procedures compared to numerical predictions of operation at the design flow speed. From the compiled experimental data, a similar trend can be observed at lower values of tip speed ratio, ranging between values of 0.4 and 2.00. This trend improves confidence in expected performance as the turbine runner rotates at lower angular velocities where less flow separation occurs and there are less chaotic shedding structures despite the flow still being fully turbulent. Fig. 14 shows similar peaks in power coefficient between experimental results and the numerical predictions of approximately 0.37 at a tip speed ratio of 2.50. Less than 3.0% relative error exists between experimental and numerical results for the prototype. This in particular validates the numerical work conducted by Riglin et al. [10,14,17–20]and Schleicher et al. [11–13,15,16]for the turbine design and characterization. More notably, the design of experiments (DOE) optimization procedures introduced and implemented by Schleicher [16] are validated and may be used for future iterations of complex blade design for other design conditions.

A sudden drop in power is observed at tip speed ratios exceeding the design point value, 2.50, regardless of channel flow speed. This sudden reduction of power is a result of the generator selection and capability. At higher tip speed ratio values, with respect to the present range of channel flow speeds investigated; the generator must operate at significantly higher voltage to keep the amperage at a manageable level. From Fig. 4, as larger voltages are experienced by the generator it becomes increasingly less likely that the amperage produced will meet the requirements specified for generator operation; specifically, a maximum of 20 A of output current. In addition to this, the generator efficiency diminishes under intense loading resulting from an increase in power output at a significantly higher generator shaft rotation rate. The present generator is capable of operating within a window of 1.0 m/s and approximately 1.9 m/s for the present blade design.

In the second test setup, the power output of the prototype was connected to a solar charging converter that mimicked the GREENS system. Loading was applied to the generator based upon how much power was being drawn from batteries. The resulting power produced when the prototype was placed under the influence of the solar charging converter is shown below in Fig. 15. Operation occurred at predominately higher rotation rates specifically at or above the optimum tip speed ratio. Comparing Figs. 15–14, a similar trend is observed at higher values of the tip speed ratio. With the presence of the solar charging converter, power production between variable loadings shows less variation compared to results with manual loading. Additionally, the power produced was conditioned and significantly less variance was observed as indicated by the marginal error bars. A stall for the propeller design occurs at a tip speed ratio between 3.6 and 3.8 regardless of testing configuration, see Figs. 14 and 15. Traditional units stall at TSR ranging from 6.0 to 8.0 depending on the design and specific

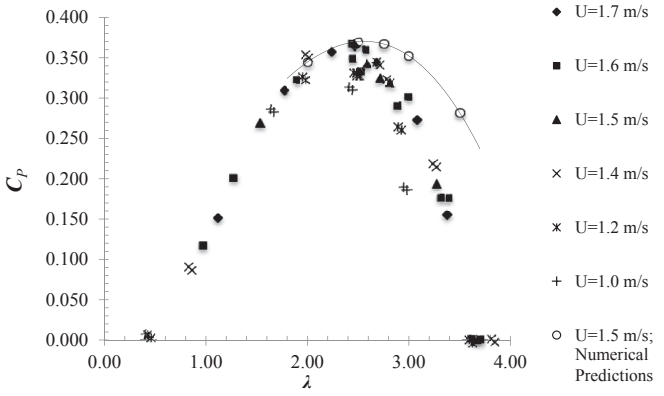

Fig. 14. Power coefficient as a function of tip speed ratio for experimental results and numerical predictions.

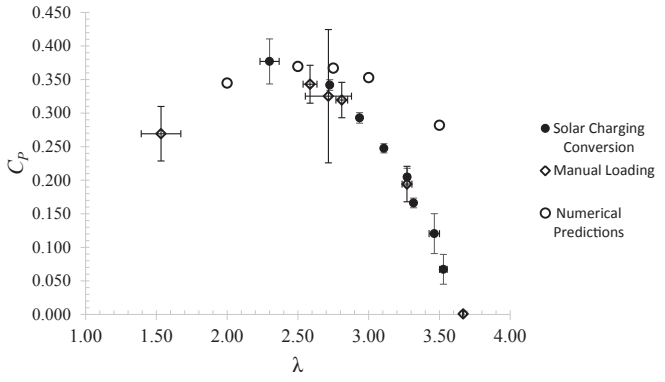

Fig. 15. Power coefficient as a function of tip speed ratio for experimental results obtained at a channel velocity of 1.5 m/s using the solar charging converter and corresponding numerical predictions.

hydrofoils used within the design. This indicates that the present unit observes boundary layer detachment at lower rotation rates while providing higher torque. The propeller design allows for lower flow rates to be used due to the high torque, low angular velocity present during operation at the cost of flexibility in blade position. Traditional units utilize blade pitch and yaw to control stall and optimum power output positions.

6. Conclusions

A hydrokinetic turbine prototype for portable, river applications was tested at the Naval Surface Warfare Center, Carderock Division. A 20 A, continuous DC generator was selected for mechanical-electrical power conversion. An inline gearbox with a 10:1 step-down gear ratio was selected to reduce the rotation rate of the generator shaft to an acceptable level for power production based upon preliminary numerical characterization and optimization of the runner design. Numerical CFD predictions were produced for the prototype with a resulting peak mechanical power coefficient of approximately 0.50 produced at a tip speed ratio of 2.50.

Testing produced two sets of experimental results: data obtained through manual generator loading and generator loading through the use of a solar charging unit. Results were obtained at flow speeds ranging from 1.0 m/s to 1.7 m/s with most results centred about the design flow speed of 1.5 m/s and a tip speed ratio of 2.75. The prototype yielded a peak power coefficient of 0.37 at a tip speed ratio of 2.50 during manual generator loading. After efficiencies of the electrical-mechanical components were applied to the mechanical power predicted through CFD analyses, a relative error of less than 3.0% was reported. The experimental work presented in the current study validates CFD analyses and optimization used in the design process by Riglin et al. [14,18–20]and Schleicher et al. [12,15,16]. Applying the solar charging converter produced results resembling those produced through manual generator loading. However, through the use of the solar charging converter, power was conditioned and showed less variability and proved that the prototype was capable of interfacing with battery systems such as the GREENS.

Funding

This project was funded by the Office of Naval Research under Award N00014-12-M-0050 through a SBIR project with e-Harvest.

Acknowledgements

The authors would like to gratefully acknowledge the Office of Naval Research and the staff at the CWC that helped with the experimental setup, channel operation, and data acquisition over the two-day testing period. The authors appreciate Robert C. Klein and e-Harvest for support and collaboration.

Notation

AR	area ratio
b	intercept, A
C	coefficient
C	capacitor,
D	diameter, m
F	blending function
GCI	grid convergence index, %
g	gravity, m/s^2
I	turbulent intensity, %
I	current, A
k	turbulent kinetic energy, J/kg
L	channel length, m
m	meridional length, m
m	slope, A/RPM
N	number of samples
P	pressure, Pa
Re	Reynolds number
r	gear ratio
S	mean rate-of-strain tensor, 1/s
t	time, s
T	thrust, N
U	velocity, m/s
$\|U\|$	velocity magnitude, m/s
V	voltage, V
$\dot{W}$	power, W
Z	quantity

Superscript

*	closure coefficient/non-dimensional
′	denotes the blade angle

Greek Symbols

α, β, σ	closure coefficients
β	relative flow angle, °
Δ	change in variable
ε	turbulent dissipation rate, m^2/s^3
ε	permutation symbol
λ	tip-speed ratio
Ω	angular velocity, 1/s
ϕ	user-defined solution quantity
θ	diffuser angle, °
Δθ	wrap angle, °
μ	dynamic viscosity, Pa-s
ν	kinematic viscosity, m^2/s
ρ	density, kg/m^3
σ	solidity
σ	standard deviation
τ	stress tensor, Pa
ω	specific dissipation rate, 1/s
η	efficiency

Subscripts

B	blades
gear	gear box
G	generator
H	hydraulic
h	at the hub
i,j,k,l,s,q,w	tensor indices
In	inside
I	current
L	electronic load
max	maximum value
Out	outside
SCC	solar charging converter
T	thrust
t	at the tip
wire	electrical wiring
∞	free stream
1,2	variable indicator

References

[1] J.J. Conti, P.D. Holtberg, J.R. Diefenderfer, A.M. Napolitano, A.M. Schaal, J.T. Turnure, L.D. Westfall, Annual Energy Outlook 2014 with Projections to 2040, U.S. Energy Information Administration, Washington, D.C, 2014.

[2] P. Jacobson, Assessment and Mapping of the Riverrine Hydrokinetic Resource in the Continental United States, Electric Power Research Institute (EPRI), Palo

Alto, CA, 2012.
[3] K. Kusakana, H.J. Vermaak, Hydrokinetic power generation for rural electricity supply: case of South Africa, Renew. Energy 55 (2013) 467–473.
[4] U.S. Geological Survey, National Water Information System Data Available on the World Wide Web (Water Data for the Nation), 2014 [Online]. Available: http://waterdata.usgs.gov/nwis/ (Accessed 09.01.14).
[5] S.S. Mukherji, N. Kolekar, A. Banerjee, R. Mishra, Numerical investigation and evaluation of optimum hydrodynamic performance of a horizontal axis hydrokinetic turbine, J. Renew. Sustain. Energy 3 (2011) 1–18.
[6] N. Kolekar, S.S. Mukherji, A. Banerjee, Numerical modeling and optimization of hydrokinetic turbine, in: ASME 2011 5th International Conference on Energy Sustainability, Washington, D.C., 2011.
[7] N. Kolekar, Z. Hu, A. Banerjee, X. Du, Hydrodynamic design and optimization of hydro-kinetic turbines using a robust design method, in: Proceedings of the 1st Marine Energy Technology Symposium, METS13, Washington D.C., 2013.
[8] N. Kolekar, A. Banerjee, Performance characterization and placement of a marine hydrokinetic turbine in a tidal channel under boundary proximity and blockage effects, Appl. Energy, 148 (2015) 121–133.
[9] J. Goundar, .M.R. Ahmed, Design of a horizontal axis tidal current turbine, Appl. Energy, 111 (2013) 161–174.
[10] J.D. Riglin, W.C. Schleicher, Z. Kraybill, R.C. Klein, A. Oztekin, Computational fluid dynamics and structural finite element analysis of a micro hydro turbine, in: ASME 2013 International Mechanical Engineering Congress and Exposition, San Diego, CA, 2013.
[11] W. Schleicher, H. Ma, J. Riglin, Z. Kraybill, W. Wei, R. Klein, A. Oztekin, Characteristics of a micro-hydro turbine, J. Renew. Sustain. Energy 6 (2014) 1–14.
[12] W. Schleicher, J. Riglin, A. Oztekin, Numerical characterization of a preliminary portable micro-hydrokinetic turbine rotor design, Renew. Energy 76 (2015) 234–241.
[13] W.C. Schleicher, J.D. Riglin, Z.A. Kraybill, A. Oztekin, Design and simulaiton of a micro hydrokinetic turbine, in: Proceedings of the 1st Marine Energy Technology Symposium, METS13, Washington D.C, 2013.
[14] J. Riglin, C. Daskiran, N. Oblas, W. Schleicher, A. Oztekin, Design and characteristics of a micro-hydrokinetic turbine system, in: Proceedings of the International Mechanical Engineering & Exposition (IMECE2015), Houston, TX, 2015.
[15] W. Schleicher, J. Riglin, A. Oztekin, R. Klein, Numerical optimization of a portable hydrokinetic turbine, in: 2nd Marine Energy Technology Symposium, Seattle, WA, 2014.
[16] W.C. Schleicher, Design Optimization of a Portable, Micro-hydrokinetic Turbine, ProQuest, Bethlehem, PA, 2015.
[17] J. Riglin, W. Schleicher, A. Oztekin, Diffuser optimization of a micro-hydrokinetic turbine, in: ASME 2014 International Mechanical Engineering Congress and Exposition, Montreal, Canada, 2014.
[18] J. Riglin, W.C. Schleicher, A. Oztekin, Numerical analysis of a shrouded micro-hydrokinetic turbine unit, J. Hydraulic Res. 53 (4) (12 July 2015) 525–531.
[19] J.D. Riglin, Design, Modeling, and Prototyping of a Hydrokinetic Turbine Unit for River Application, ProQuest, Bethlehem, PA, January 2016.
[20] J. Riglin, W. Schleicher, I. Liu, A. Oztekin, Characterization of a micro-hydrokinetic turbine in close proximity to the free surface, Ocean. Eng. 110 (1 December 2015) 270–280.
[21] J. Riglin, C. Daskiran, J. Jonas, W.C. Schleicher, A. Oztekin, Hydrokinetic turbine array characteristics for river applications and spatially restricted flows, Renew. Energy, 97 (2016) 274–283.
[22] C. Daskiran, J. Riglin, A. Oztekin, Computational study of multiple hydrokinetic turbines: the effect of wake, in: ASME 2015 International Mechanical Engineering Congress and Exposition, Houston, Texas, 2015.
[23] P. Mycek, B. Gaurier, G. Germain, G. Pinon, E. Rivoalen, Experimental study of the turbulence intensity effects on marine current turbines behaviour. Part II: two interacting turbines, Renew. Energy, 68 (2014) 876–892.
[24] P. Mycek, B. Gaurier, G. Germain, G. Pinon, E. Rivoalen, Experimental study of the turbulence intensity effects on marine current turbines behaviour. Part I: one single turbine, Renew. Energy 66 (June 2015) 729–746.
[25] A.S. Bahaj, A.F. Molland, J.R. Chaplin, W.M.J. Batten, Power and thrust measurements of marine current turbines under various hydrodynamic flow conditions in a cavitation tunnel and a towing tank, Renew. Energy, 32 (2007) 407–426.
[26] F.-F. Li, J. Qiu, Multi-objective optimization for integrated hydro-photovoltaic power system, Appl. Energy 167 (1) (2016) 377–384.
[27] D. Cebrián, J.F.-F.R. Ortega-Casanova, Lift and drag characteristics of a cascade of flat plates in a configuration of interest for a tidal current energy converter: numerical simulations analysis, J. Renew. Sustain. Energy 5 (2013) 1–19.
[28] F. R. Menter, Zonal Two-equation K-ω Turbulence Models for Aerodynamic Flows, AIAA Paper 93-2906.
[29] F.R. Menter, Two-equation eddy-viscosity turbulence models for engineering applications, AIAA J. 32 (8) (1994) 1598–1605.
[30] D.C. Wilcox, Turbulence Modeling for CFD, DCW Industries, Inc., La Canada, California, 2010.
[31] P.J. Roache, A method for uniform reporting of grid refinement studies, in: Proceedings of the 11th AIAA Computational Fluid Dynamics Conference, Orlando, 1993.
[32] P.J. Roache, Perspective: a method for uniform reporting of grid refinement studies, ASME J. Fluids Eng. 116 (3) (1994) 405–413.
[33] P.J. Roache, Quantification of uncertainty in computational fluid dynamics, Annu. Rev. Fluid Mech. 29 (1997) 123–160.
[34] I. Celik, C.J. Chen, P.J. Roache, G. Scheurer, in: Symposium on Quantification of Uncertainty in Computational Fluid Dynamics, in FED-ASME, New York, 1993.
[35] H. Saunders, C. Hubbard, The circulating water channel of the david w. taylor model basin, SNAME Trans. 52 (1944).

Additive Manufacturing 16 (2017) 115–123

Contents lists available at ScienceDirect

Additive Manufacturing

journal homepage: www.elsevier.com/locate/addma

Full Length Article

Wire and arc additive manufactured steel: Tensile and wear properties

C.V. Haden*, G. Zeng, F.M. Carter III[1], C. Ruhl, B.A. Krick, D.G. Harlow

Department of Mechanical Engineering and Mechanics, Lehigh University, Bethlehem, PA 18015, USA

ARTICLE INFO

Article history:
Received 20 June 2016
Received in revised form 18 April 2017
Accepted 21 May 2017
Available online 23 May 2017

Keywords:
3D printing
Steel
Wear
Strength
Focused ion beam
Microscopy

ABSTRACT

The present study systematically investigated the mechanical properties of wire-based (wire and arc additive manufacturing, known as WAAM) deposition of steel metals, both stainless steel 304 and mild steel ER70S. Graded material properties of stainless steel 304 were observed for wear and hardness in the direction of deposition and in Z height, due to variations in local thermal histories of the metal. Wear rates decreased significantly ($p = 5.6 \times 10^{-12}$ by one-way ANOVA) along the length of the deposited material, from $K = 2.62 \times 10^{-5}$ mm^3/N m (+/− 2.32×10^{-6} mm^3/N m), to $K = 0.63$ mm3 x 10^{-5} mm3/N m (+/−3.08 x 10-6 mm^3/N m), whereas microhardness values increased significantly ($p \sim 0$ by one-way ANOVA) along the same path from $\mu = 202.3$ HV and $\sigma = 5.82$ HV to 210.9 HV and $\sigma = 5.91$ HV. The yield and ultimate strength, however, were not found to be statistically significantly different ($p = 0.55$) along the direction of deposition for SS304. During wear testing, a grain refinement was observed directly beneath the wear scar in these materials in a focused ion beam channel observed under scanning electron microscopy. Additionally, no significant difference in yield strength was observed in printed mild steel (ER70S) between vertical and horizontal specimens. The observed graded mechanical properties in stainless steel 304 allow the opportunity for varying the processing conditions to design parts with locally optimized or functionally graded mechanical properties.

1. Introduction

Additive manufacturing (AM), commonly known as 3D printing, refers to the layer by layer construction of parts from raw materials, as opposed to traditional subtractive manufacturing. In particular, AM of metals via wire and arc additive manufacturing (WAAM) technologies uses a welding wire feedstock to build components, which Williams et al. reported is both inexpensive and commercially available, allowing the technology to be economical [1]. In addition, the multi-pass welding process reduces material waste and offers much faster speeds than powder bed AM, according to a study by Martina et al. which investigated the benefits of WAAM technology [2]. However, a greater understanding of the resulting material properties for this type of deposition is still needed before the production of reliable critical load bearing parts becomes mainstream.

The effect of WAAM on the material properties of steels is poorly characterized to date. Most recent studies have investigated deposition schemes, reliable printing parameters and performed feasibility studies. Xiong et al. first worked on controlling deposited bead width [3], then in 2014 Xiong and Zhang demonstrated an adaptive control system for consistent nozzle height position relative to the previous weld line. Most recently [4], Xiong et al. have integrated a closed-loop control of the deposition process [5], while Ding et al. have worked to develop a gas shielding device for their WAAM system [6].

A handful of groups are currently looking at the resulting material properties of WAAM metals, including Simhambhatla et al. [7] who studied the anisotropic tensile properties and hardness of mild steel produced from hybrid layered manufacturing (HLM), an approach which alternates the use of gas metal arc welding (GMAW) and computer numerical control (CNC) machining process to produce parts. Their findings revealed the number of heating cycles experienced by the metal correlates inversely with hardness. In other words, the final few layers deposited in WAAM at the top of a part experience fewer thermal cycles, leading to improved hardness of the material. The residual effects of welding passes do not reach deeper than 5 layers, according to their simplified models, and only the top few layers have increased hardness. Their group proposed that thermal cycling causes annealing and softening in adjacent affected layers. Further research by Colegrove et al. [8] demonstrated successful improvement of the microstructure of WAAM mild steel via grain refinement and released residual

* Corresponding author.
E-mail address: christina.haden@lehigh.edu (C.V. Haden).
[1] Present address: Sciaky Global Headquarters, Sciaky, Inc. 4915 W 67th St. Chicago, IL 60638, USA.

http://dx.doi.org/10.1016/j.addma.2017.05.010
2214-8604/

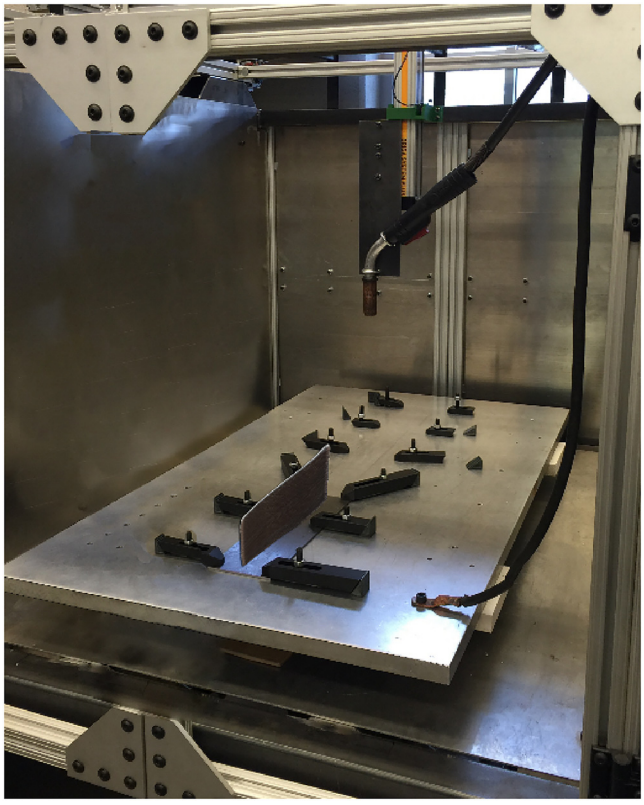

Fig. 1. Lehigh University's 3D metal printer using WAAM.

stresses near the baseplate (which is a known challenge of the WAAM approach) using high-pressure rolling. Ding et al. [9], on the other hand, modeled the thermo-mechanical properties of mild steel WAAM structures to predict their residual stresses and associated distortion.

In an effort to characterize the optimal processing conditions for improved cladding, a large body of work exists which observed the characteristics of single and multi-pass weld lines. For example, work by Murugan and Parmar in 1997 [10] investigated the metallurgical features of welded stainless steels. However, to the best knowledge of the authors, no research has yet been published on the wear, hardness and yield properties of deposited stainless steels as they relate to additive manufacturing via WAAM. The research performed herein describes the mechanical properties observed on both stainless (304) and mild (ER70S) steels produced via this process.

2. Experimental setup: machine preparation, materials and methods

All samples were prepared using an in-house WAAM printing instrument (Fig. 1) inspired by Anzalone et al. who first demonstrated the feasibility of a low-cost open-source metal 3D printer [11]. The 3D metal WAAM printer at Lehigh University is currently configured with a Millermatic 250 gas metal arc welder (Miller Electric Manufacturing Co.) and a roughly 0.5^3 m Cartesian gantry positioning system (Macron Dynamics, Inc. and Parker Origa OSP-E25). The welding nozzle position is determined from CNC commands derived from a computer aided design (CAD) rendition of the desired part. The part is converted using open source software Slic3r engine (slic3r.org) to GCODE which dictates motion commands to the microcontroller. The deposited metal is printed directly onto 6.35 mm thick metal plates secured to a large stationary aluminum jig plate (1140 mm × 680 mm × 25 mm) via step clamps. The jig plate is electrically isolated from the frame of the machine and serves as the grounded connection to complete the arc welding circuit.

2.1. Stainless steel 304 prints

A single weld line wall (shown in Figs. 1 and 2, left) was deposited on a stainless steel (grade 304) build Plate 6.35 mm thick using a standard stainless steel welding wire grade ER308 LSI (0.889 mm diameter) supplied by Airgas USA, LLC. The welder operated at 22 V and 5435 mm/min (or 214 IPM) wire feed rate with a variable current for the entirety of the build, with a nozzle travel speed of 152 mm/min. The printed wall final dimensions are approximately 380 mm in length by 115 mm in height by 6.35 mm thick. Each weld line was deposited in the same direction, producing a surplus of material at the beginning of lines and a weld runoff at the end of the weld deposition passes (seen also in Fig. 2). A tri-gas mixture composed of 90% Helium, 7.5% Argon and 2.5% CO_2 was used as shielding gas during deposition with a gas flow rate of 44 CFH.

2.1.1. Specimen preparation

The specimen cut plan is shown as an overlay of the wall in Fig. 2. Three square samples were taken near the mid-line height of the wall at the beginning (MB), middle (MM) and end (ME) of the part in the horizontal build direction. These samples were mounted in a phenolic resin (Bakelite) with the top surface polished using gradually finer grit papers and finishing with a 0.05 μm diameter silicon dioxide bead polishing slurry. The surface perpendicular to the direction of build, as shown in Fig. 3, was observed on the MB, MM and ME specimens. These mounted and prepared specimens were then used for microscopy, wear testing and microindentation hardness testing.

2.1.2. Uniaxial tensile testing

A total of eight horizontal tensile specimens (Fig. 2, TB1-TB8) were cut from the stainless steel wall to subsize specimen dimensions according to ASTM A370-13 with gauge dimensions of 6.1 mm wide by 2.54 mm thick by 25.4 mm in length. Tensile testing was carried out on an Instron/MTI electromechanical test frame (Instron TTC, 4500 kg capacity), by applying a constant 1.5 mm per minute crosshead displacement.

2.1.3. Micro-indentation hardness testing

Vickers hardness tests for samples MB, MM and ME were carried out on a AMH43 Automatic Microindentation Hardness Testing System (LECO Corporation). A single weld bead measures on average 1.8 mm in vertical height, allowing a total of approximately 12 weld lines to be visible on each specimen (MB, MM and ME). The microhardness tests on MB and ME were line tests spanning four weld lines with a total of 100 points, whereas the MM sample was covered with 240 points in a rectangular grid covering an area 2.2 mm by 4.7 mm for greater spatial resolution.

2.1.4. Wear testing

The material wear rate (K, in $\frac{mm^3}{N \cdot m}$) was determined for the printed stainless steel samples MB, MM and ME to compare nominally identical material deposition conditions. Wear measurements were conducted on a custom microtribometer, as previously described by Krick et al. [12]. A single crystal ruby probe with a diameter of 3 mm was reciprocated against the stainless steel sample with a constant speed of 1 mm/s. The applied normal load was 100 mN (maximum Hertzian contact pressure ~0.6 GPa). The cross-sectional area of the wear scar was determined by optical profilometer and the Archard wear rate (recently described by Erickson

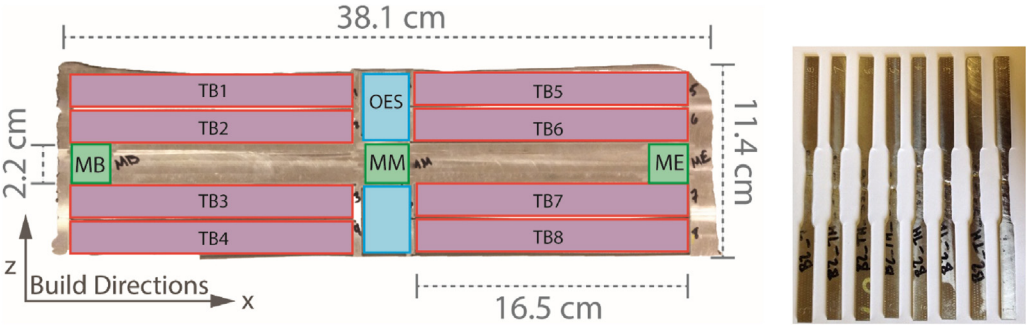

Fig. 2. Left: Picture of the stainless steel build with overlaid specimen cut plan. The horizontal tensile bar blanks (TBX), Bakelite mounted specimen blanks (MX) and optical emission spectroscopy (OES) blanks are shown. Right: Machined tensile specimens (TB1-TB8) are shown.

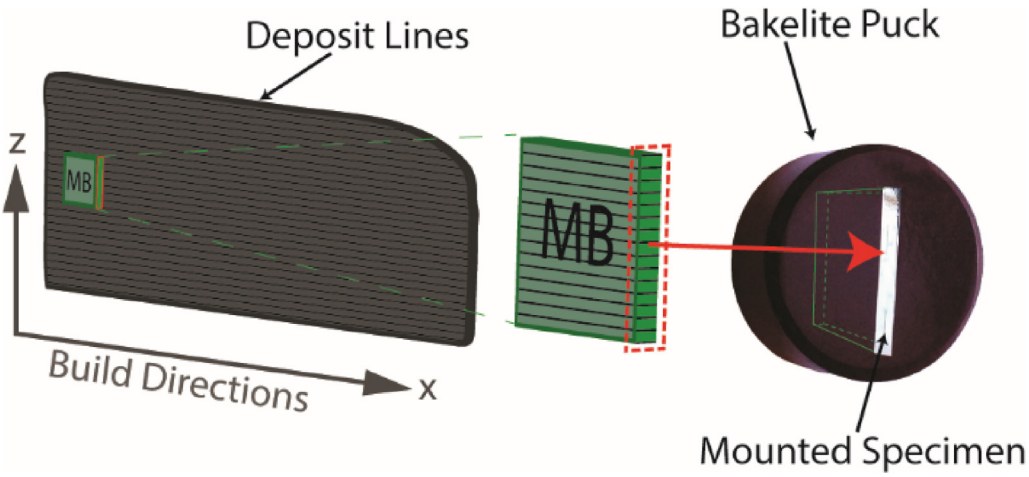

Fig. 3. Example specimen mounting direction within Bakelite resin mounts. Surface highlighted was observed using light and scanning electron microscopy, as well as used for microhardness and wear testing.

et al. [13]) was reported for 10,000 reciprocating cycles (20,000 sliding passes). The wear scar was performed parallel to the Z-height direction of the deposited material, and spanned several weld lines.

2.1.5. SEM and FIB

Grain refinement induced by applied load during the wear test was interrogated by FIB and SEM. A region of interest within the wear scar was first coated with a 2 μm thick platinum layer, in order to protect the worn surface. A 25 μm long by 15 μm wide trench was made by FIB milling (FEI Scios) with 65 nA ion beam current at 30 kV. Next, the beam current was gradually dropped to 1 nA to successively refine the cut and minimize the curtain effect within the trench, to observe the grain structure immediately below the wear scar.

2.2. Mild steel ER70S-6 prints

A second wall measuring approximately 21.6 cm in length by 11.5 cm in height and 0.6 cm in thickness was produced from standard welding wire of grade ER70S-6 (0.889 mm diameter, also supplied by Airgas USA, LLC) and deposited onto a Plate 6.35 mm thick of mild steel grade A36, which is a material nearly compositionally identical to the welding wire. The welder operated at 19 V and 5080 mm/min (or 200 IPM) wire feed rate with a variable current for the entirety of the build, with a nozzle travel speed of 152 mm/min. Each bead was layered in the same direction, as shown by the build direction arrows in Fig. 4. A 75% Argon and 25% CO_2 gas mixture was used as the shielding gas during deposition with a gas flow rate of 30 CFH. The specimen cut plan (overlay

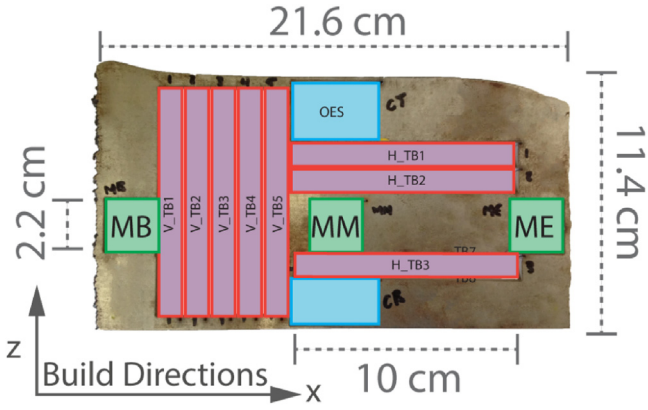

Fig. 4. Picture of mild steel (ER70S) printed wall and overlaid specimen cut plan. Horizontal and vertical tensile bar blanks (H-TBX and V-TBX, respectively) are also indicated.

in Fig. 4) produced three square samples taken near the mid-line height of the wall (MB, MM and ME) similar to those samples taken from the stainless steel wall. These samples were also mounted in Bakelite resin and polished for microscopy, wear testing and microindentation hardness testing as described above. The vertical and horizontal specimen blanks (V-TBX and H-TBX, respectively) were also machined for tensile testing according to ASTM A370-13.

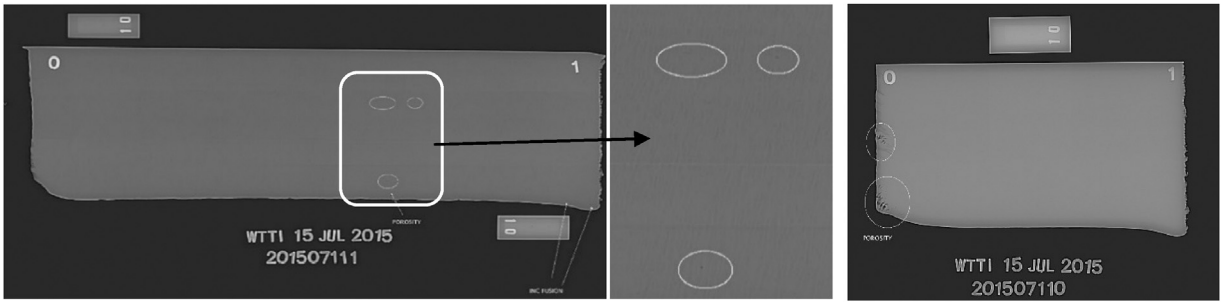

Fig. 5. X-ray graph of the deposited stainless steel (left) and mild steel (right) walls.

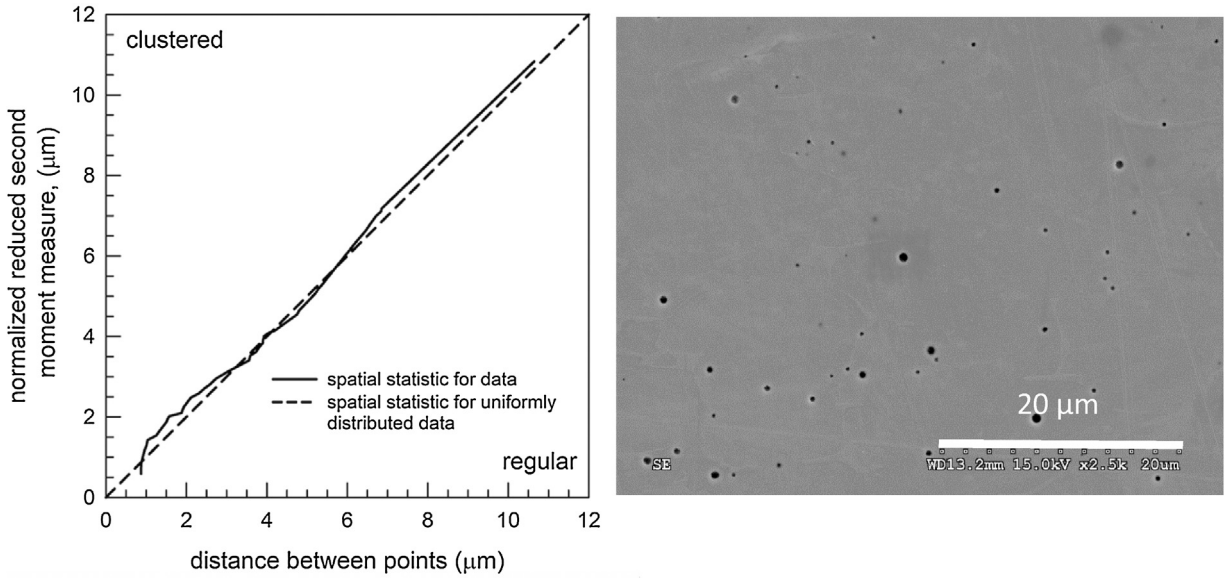

Fig. 6. Right: SEM image of the polished surface of printed stainless steel with porosity in dark circles. Left: the statistical analysis of spatial distribution on the pores seen in the SEM.

Table 1
Optical Emission Spectroscopy (OES) composition analysis was performed on the stainless steel printed metal. The printed metal (first column) is compared to 304 and 308 reference composition standards.

Element	Printed Metal	Ref. 308	Ref. 304
C	0.02	0.08 Max	0.08 Max
Cr	19.74	19.00–21.00	18.00–20.00
Mn	1.68	2.00 Max	2.00 Max
Ni	9.36*	10.00–12.00	8.00–10.50
P	0.029	0.045 Max	0.045 Max
S	0.018	0.030 Max	0.030 Max
Si	0.76	1.00 Max	1.00 Max
Cu	0.25	–	–
Mo	0.20	–	–

3. Results and discussion

3.1. Composition analysis

A material specimen from the stainless steel wall was prepared for optical emission spectroscopy (OES, Fig. 2). This chemical composition analysis test was performed by IMR Test Labs in Lansing, NY to determine whether the composition of the newly produced material was different from that of the feedstock wire. According to this analysis (see Table 1 below), the sample meets the requirements of UNS-S-30400 for an AISI 304 chromium-nickel stainless steel, but fails that of UNS-S-30800 because of the Ni content in the build. The certificate of analysis provided with the raw wire material indicated the stainless steel started with 10.31% composition of Nickel. Together with the OES analysis, these data indicate the stainless steel metal composition may have changed slightly during deposition. Henceforth, all results on the printed stainless steel wall will be compared to the wrought properties of type 304.

3.2. Porosity

The stainless steel and mild steel walls were first analyzed by WTTI (Welder Training & Testing Institute, Inc.) by X-ray to determine gross macroscopic porosity (Fig. 5). Very little porosity was visible in the X-ray images, with a total of three defects visible on the millimeter scale for the stainless steel wall, as highlighted in the center image of Fig. 5. Some visible defects at the end of the line on the mild steel were the result of slag accumulation.

The polished surface of the stainless steel sample MM was observed under scanning electron microscopy (Hitachi 4300 SE/N) to further investigate sub-millimeter sized pores which were not visible in the X-ray images. The specimen image (Fig. 6, right) contained 58 visible pores averaging 0.36 μm in diameter. Pore sizes and positions were extracted from the digital image for further statistical analysis using ImageJ software, which was developed by Abramoff et al. [14].

A spatial statistical analysis was performed to determine whether there was a preferential distribution of these pores. This

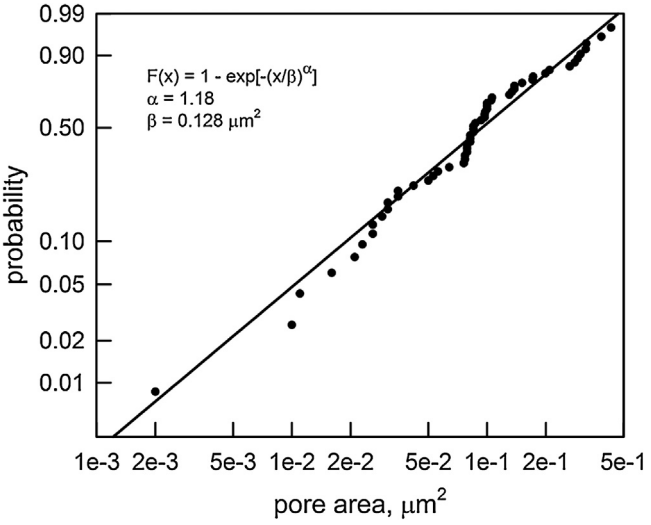

Fig. 7. Probability distribution of pore sizes on Weibull paper.

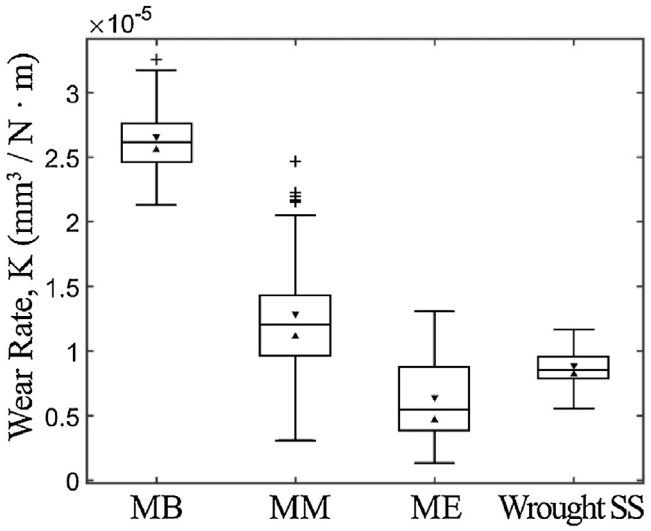

Fig. 9. Wear rates reported for the beginning (MB), middle (MM) and end (ME) regions of the stainless steel printed material, as compared to wrought stainless steel 304.

type of analysis was demonstrated previously by Harlow et al. [15], and is based on an excellent survey of spatial point processes described by Diggle [16]; specific details of the analysis and definition of the technical terms used below can be found there. For the observed pores, the results are shown on the graph in Fig. 6 (left). The vertical scale has been normalized so that the diagonal line is for the completely spatially random (CSR) model. Clearly, the pores are well represented by the CRS model because the statistical estimate of the normalized reduced second moment measure for the data is nearly identical to that for the CRS model. Consequently, there is no preferential aspect in the build process that produces the pores, at least in the observed image, and the pore distribution appears to be uniformly randomly generated at this particular location.

Furthermore, the distribution of the areas of the 58 pores are shown on Fig. 7. The graph is shown on two parameter Weibull probability paper. Since the data are linear, a two parameter Weibull distribution, the form of which is described on the figure, is an acceptable characterization for the data. The linear fit is the maximum likelihood estimate (MLE) for the data, and the MLE estimated parameters are also shown on the figure. The Kolmogorov – Smirnov and Anderson – Darling goodness of fit tests indicate that the MLE estimate is acceptable for any significance level less than 20%. Consequently, the MLE estimate is a very good characterization for the data. Moreover, the MLE estimates for the pore surface area mean and coefficient of variation are $\mu = 0.121$ μm2 and cv = 85.0%, respectively. Even though the pore sizes are relatively small, there is significant variability in the sizes, which span 3 orders of magnitude.

3.3. Grain size and orientation

The grain sizes and orientation of the same MM stainless steel sample was further observed by electron backscatter diffraction (EBSD) using a Hitachi 4300 SE/N system. Fig. 8 shows the EBSD map and corresponding grain size plot. The EBSD map shows randomly oriented grains with grain sizes ranging between 0.003 mm^2 and 0.75 mm^2. Grains with sizes mostly in the range of <100 μm to 300 μm are seen in Fig. 8a. This microstructure characterization will be used for later comparison with stress-induced grain refinement.

3.4. Wear studies

Wear rates on the stainless steel printed material were determined using the method described earlier. As seen in Fig. 9, wear rate is a function of location on the printed sample. Wear rate is highest at the beginning of the print path (MB) monotonically decreasing in the direction of weld line deposition from the begin-

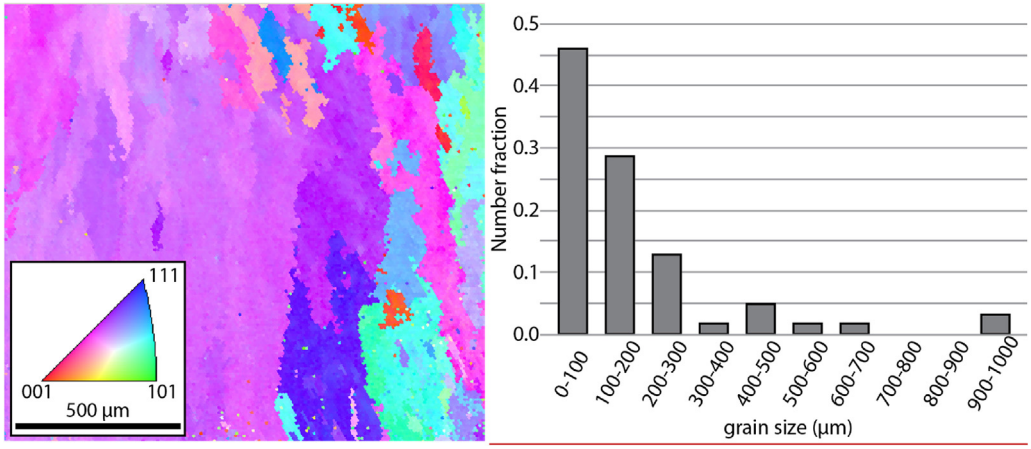

Fig. 8. Electron back scatter diffraction (EBSD) of the surface of stainless steel and corresponding grain size plot.

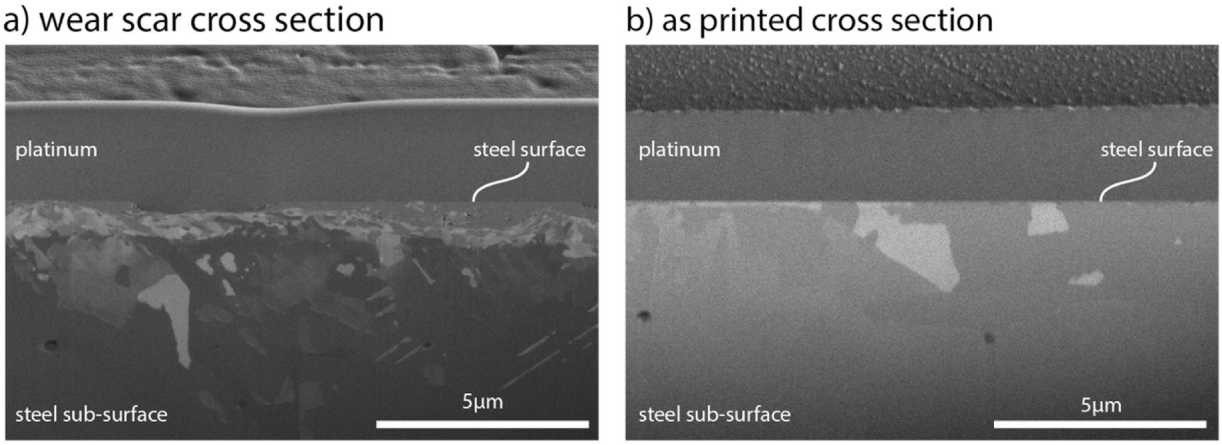

Fig. 10. SEMs of the cross-sectional view of stainless steel printed materials a) directly beneath a wear scar and b) as printed samples.

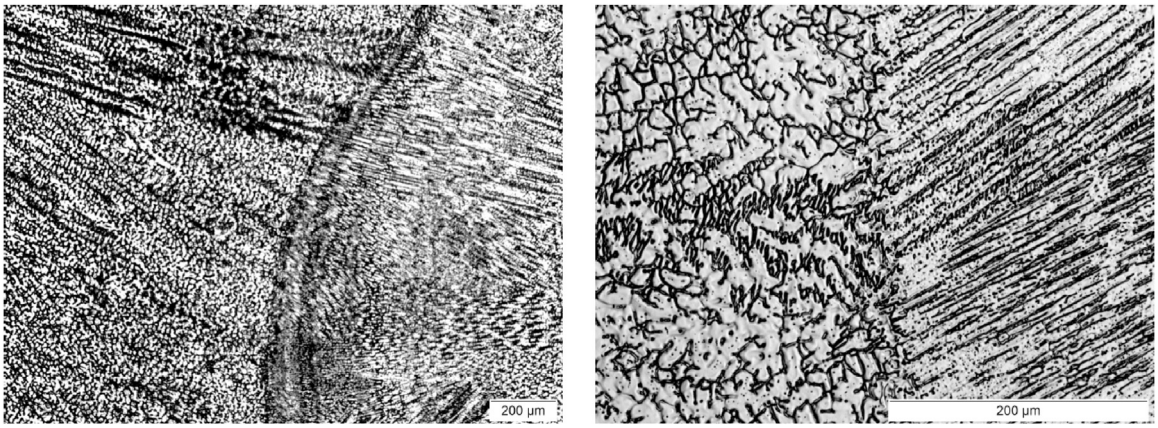

Fig. 11. Optical micrographs of the interfacial layer between weld lines (left) and repeating microstructural shifts observed near weld interfaces, both in AM stainless steel 304. Direction of increasing z-height is horizontally to the left.

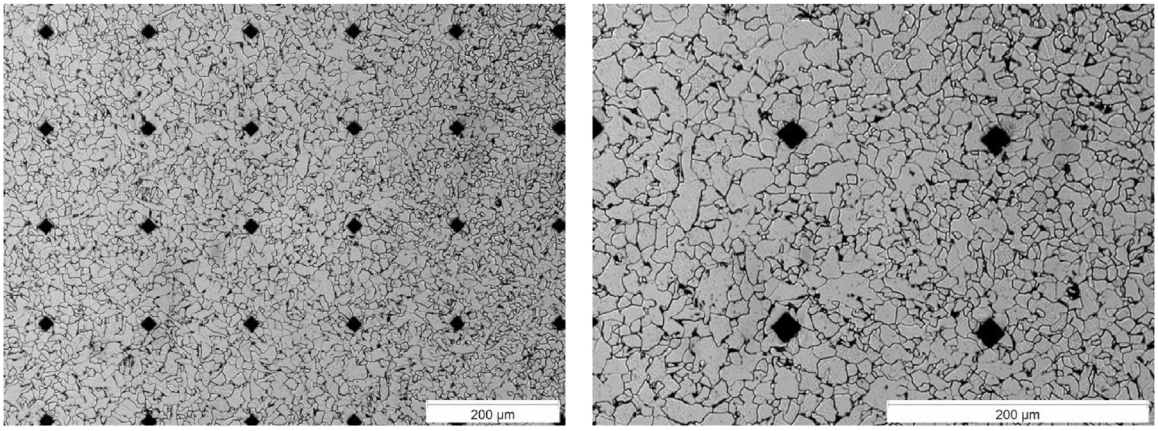

Fig. 12. Optical micrographs of a representative microstructure in AM mild steel ER70S-6. Direction of increasing z-height is horizontally to the left.

ning to the end of the sample. The differences observed between each of the samples (MB, MM and ME) were statistically significant ($p \sim 0$ bye one-way ANOVA and Tukey-Kramer post hoc analyses), indicating the material wear resistance is graded along the deposition direction. A comparison to wrought stainless steel material indicated the printed ME performed slightly better than wrought material, with MB reporting as a slightly less wear resistant material than wrought. This trend suggests that the wear performance depends on material microstructure, which varies with weld path location. From this trend of varying wear resistances, in a practical setting, print parameters could be engineered to optimize the local wear resistance of critical part features.

3.5. SEM and FIB milling

To further characterize the importance of the stainless steel microstructure and its evolution during sliding, scanning electron microscopy (SEM) and focused ion beam (FIB) milling were

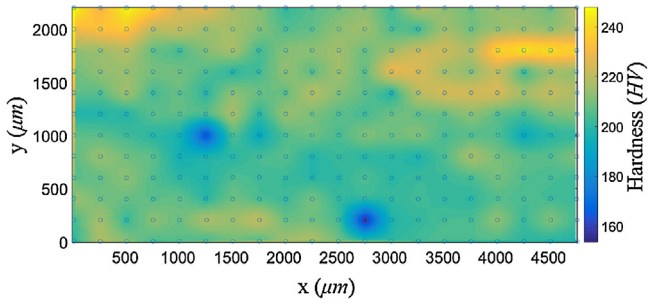

Fig. 13. Contour plot of the interpolated hardness on the surface of stainless steel.

employed to observe the MM stainless steel surface immediately below the wear scar. A cross-sectional view of the steel surface and subsurface is revealed by imaging the side of the trenches both within the wear scar (Fig. 10a) and on an unworn control sample in another region of the stainless steel (Fig. 10b). As seen, the surface immediately below the wear scar underwent significant grain refinement as compared to Fig. 10b. The grain size deeper in the FIB channel beneath the wear scar is consistent with that seen below the surface in the control region. Wang and Li found that the grain refinement (Hall-Petch strengthening) seen beneath the wear scar is typical for stainless steel, and impedes dislocation movement, and thus increases the yield strength of the material [17]. This provides further evidence that the printed stainless steel material exhibits a similar mechanical response in the presence of external shear loading to conventional steels.

3.6. Optical microscopy

Optical micrographs were obtained from the ME stainless steel samples. A microstructure delineation is visible at the weld line interface, as seen in Fig. 11 on the left. However, within the same ME sample, mixed modes of solidification visibly result in a variety of microstructures, from austenitic to solidification structures with mixed ferrite morphology. The abrupt texture changes within the microstructure imply the local thermal histories may play a significant role on anisotropy (Fig. 12).

Optical micrographs for the mild steel ER70S-6 MM sample offer a representative microstructure seen throughout the build. A typical ferrite microstructure is seen with small regions of pearlite at the grain boundaries. Grain coarsening is observed in some areas, but no clear delineations are observed at this scale between weld layers. Repeating diamond shape patterns seen are the result of micro-indentation hardness testing.

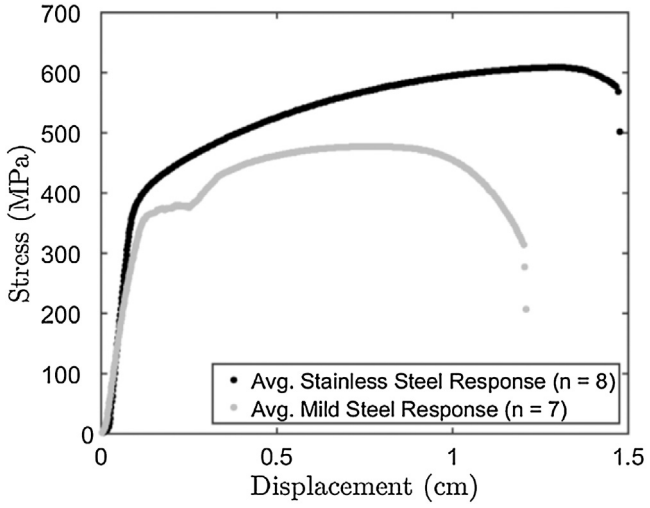

Fig. 15. Stress-displacement curves for stainless steel and mild steel specimens.

3.7. Micro-Indentation hardness

To further investigate the microstructural variability and its effect on material properties, micro-indentation hardness studies were performed on these materials. Typically, stainless steel 304 has a Vickers Pyramid Number (HV) of 129 and a yield strength of 215 MPa. The mean HV recorded on the MB, MM and ME printed stainless steel samples were 202.3, 209.2 and 210.9, respectively, and were statistically different from one another ($p \sim 0$ by one-way ANOVA). These data confirm the lengthwise hardening trend with wear testing, meaning an incrementally stronger material occurs along deposition direction. A general relationship, originally determined by Arbtin and Murphy [18] in 1953 and later updated [19] relates the material hardness and yield strength, by $HV = 3 \cdot \sigma_y$, implying material yield strength might also vary along the length of the material.

The open circles in Fig. 13 represent the location of Vickers probe indentations, covering an area 2.2×4.7 mm on the MM sample of SS304. Although the area spans three weld lines, no weld line hardness patterns are visible. It is hypothesized that the spatial density of the grid on the micron order was insufficient to capture weld line hardness variations, and nanoscale indentation will be required to further investigate the weld line material properties. Boxplot representations of the mean hardness for the MB, MM and ME hardness tests are shown in Fig. 14, left. A one-way ANOVA showed the means of each are statistically significantly different from one another, with $p < 0.05$. The population of each sample

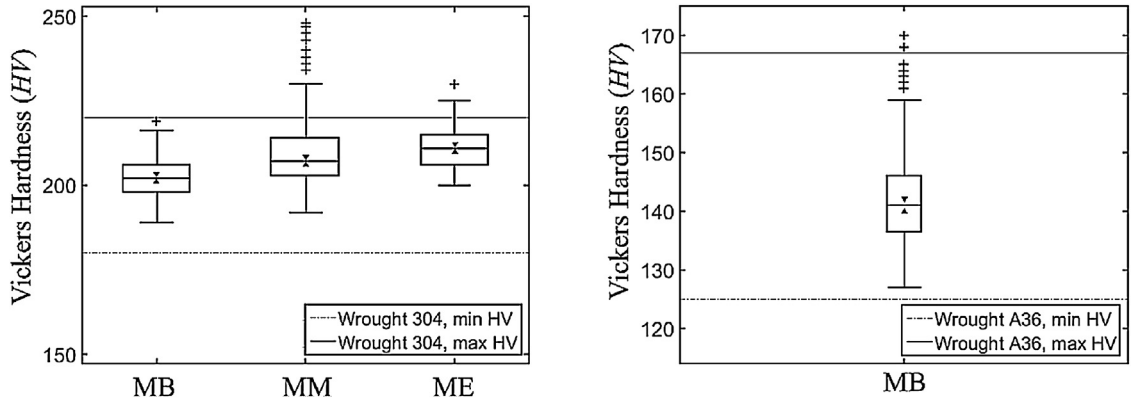

Fig. 14. Left: Boxplot showing the microhardness data of MB, MM and ME stainless steel samples. Right: Boxplot showing the microhardness data of the MB sample in mild steel.

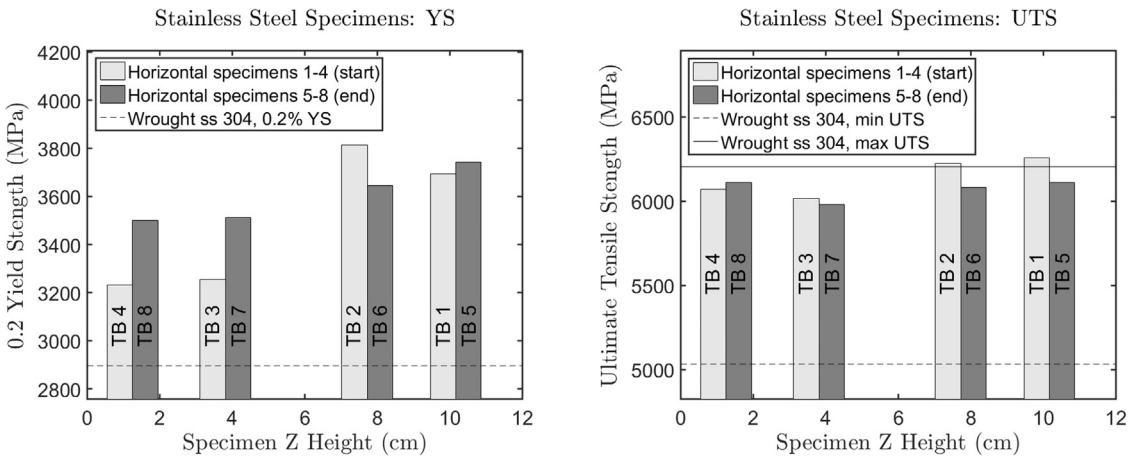

Fig. 16. Yield strength (left) and ultimate tensile strength (right) of printed stainless steel 304 specimens (TB1-8) at varying Z heights in the wall.

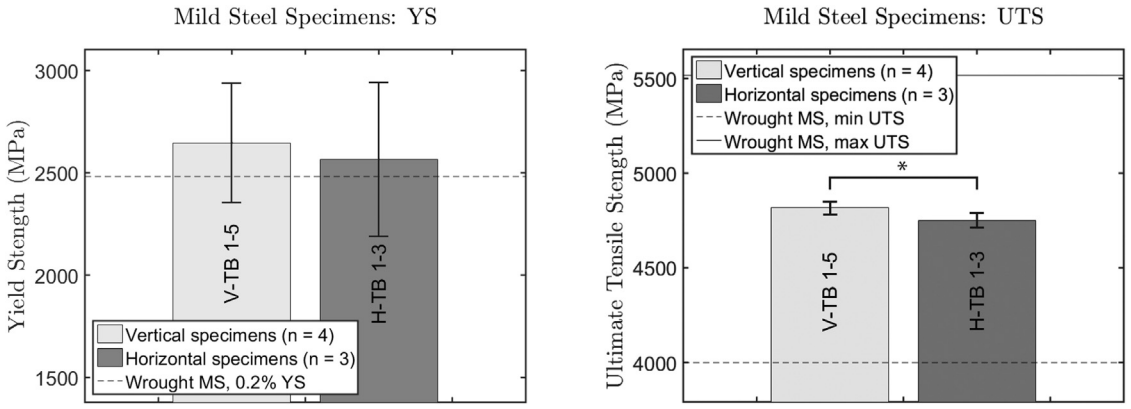

Fig. 17. Yield strength (left) and ultimate tensile strength (right) of printed mild steel (ER70S) specimens (V-TBX and H-TBX).

hardness was approximately normally distributed, warranting the ANOVA test. Minimum and maximum values for wrought stainless steel 304 material were obtained from Wang and Li [17], and shown as a comparison in Fig. 14, left. As seen, the printed stainless steel samples fall within, or slightly exceed, the wrought material expected hardness, reinforcing the material hardening along the deposition direction observed with wear testing.

In mild steel, a single line microhardness test was performed on the MB sample, to understand how material strenght of the printed ER70S compared to wrought. These results are shown by the boxplot in Fig. 14, right. The printed mild steel material has an average value falling between the minimum and maximum values for wrought ASTM A36, which is compositionally nearly identical to ER70S-6.

3.8. Uniaxial tensile testing

Since many design criteria are based on the yield and ultimate tensile strength of materials, tensile tests were performed on the printed stainless and mild steel materials to determine how they compare to wrought materials. For the stainless steel specimens, a linear elastic region was seen at onset of load application (Fig. 15, black line), with a yield strength which exceeds that of wrought 304 stainless steel (Fig. 16, left). When comparing specimens taken at different locations within the walls (see Fig. 2), an increasing yield strength trend is observed both in the direction of weld deposition (X-direction) and in height (Z-direction). These differences in yield strength, particularly between the lower and upper specimens in the wall, suggest local thermal history and resulting mode of solidification, have a significant impact on the material properties variability, and reinforce work by Simhambhatla et al. [7], who found cyclic heating caused annealing and softening of adjacent layers. The ultimate tensile strength (UTS, Fig. 16, right) for the printed stainless steel falls within (or slightly exceeds) the UTS range for wrought stainless steel 304. Here, however, a more modest increase in UTS is observed between the lower and upper half of the wall, with nearly identical responses between the start and end of lines for the lower half of the wall. These results suggest the UTS of WAAM stainless steels may be more robust to thermal history experienced by the material, however, more specimens will be required for statistical significance. None-the-less, these findings suggest careful toolpath planning may be used to control and design localized material properties in the WAAM process.

In the mild steel specimens, an elastic region was seen at onset of load application, followed by inhomogeneous yielding at the elastic/plastic transition (Fig. 15, grey line). This behavior was found to be typical for low carbon steels by Young et al. [20]. The upper yield strength is reported here as the yield strength of these materials. The printed mild steel yield strength is very similar to that of wrought A36 stainless steel (Fig. 17, left), and the vertical and horizontal specimens do not display a statistically significant difference, implying isotropic material properties, however more specimens will need to be tested for statistical power. Mild steel UTS on the other hand, fell directly between the minimum and maximum expected values (Fig. 17, right), with a statistically significant ($p = 0.05$) difference between the horizontal and vertical specimens.

These data in both stainless and mild steel suggest careful toolpath planning can be used to control and design localized material properties in the WAAM process.

4. Conclusions

Mild and stainless steels were used to build nominally rectangular specimens using WAAM. The goal of this effort was to investigate typical material properties of the builds compared to similar wrought materials. The in-house printer is quite effective for simple builds. This is confirmed by the CSR porosity and the small sizes of the pores. In addition, a declining wear rate occurs in the direction of the weld deposition in stainless steels, indicating that the material wear resistance and strength are graded along the deposition path. Hall-Petch strengthening was observed under wear scars on the stainless steel build, indicating grain refinement is occurring in this material. Abrupt texture changes are visible using light microscopy, however, these do not correlate to significant local variations in hardness. However, macroscopic hardness is significantly different and graded from the beginning to the ends of the stainless steel printed wall. In mild steel, however, no significant difference was observed in yield strengths between horizontal and vertical specimens. These experiments help formulate a research plan to more fully characterize the resulting material properties of WAAM printed metals. Further investigation will require vertical and horizontal specimens from stainless steel to determine whether a difference appears in this material between vertical and horizontal specimens. For appropriate statistical characterization, a larger number of specimens will be required. In addition, given the importance of solidification modes on material behavior, the thermal history of future builds will be investigated.

Acknowledgements

This work was supported by the Commonwealth of Pennsylvania, Department of Community and Economic Development (Grant No.: C000053981), and the Air Force Research Laboratory under agreement number FA8650-12-2-7230. The U.S. Government is authorized to reproduce and distribute reprints for Governmental purposes notwithstanding any copyright notation thereon. The views, opinions, findings, conclusions or recommendations expressed herein are those of the authors and do not necessarily reflect the views, official policies or endorsements, either expressed or implied, of Air Force Research Laboratory, the U.S. Government, the Commonwealth of Pennsylvania or Carnegie Mellon University.

References

[1] S.W. Williams, F. Martina, A.C. Addison, J. Ding, G. Pardal, P. Colegrove, Wire + Arc additive manufacturing, Mater. Sci. Technol. (2016) 1–7.
[2] F. Martina, J. Mehnen, S. Williams, P. Colegrove, F. Wang, Investigation of the benefits of plasma deposition for the additive layer manufacture of Ti-6Al-4 V, J. Mater. Process. Technol. 212 (2012) 1377–1386.
[3] J. Xiong, G. Zhang, Z. Qiu, Y. Li, Vision-sensing and bead width control of a single-bead multi-layer part: material and energy savings in GMAW-based rapid manufacturing, J. Clean. Prod. 41 (2013) 82–88.
[4] J. Xiong, G. Zhang, Adaptive control of deposited height in GMAW-based layer additive manufacturing, J. Mater. Process. Technol. 214 (4) (2014) 962–968.
[5] J. Xiong, Z. Yin, W. Zhang, Closed-loop control of variable layer width for thin-walled parts in wire and arc additive manufacturing, J. Mater. Process. Technol. 233 (2016) 100–106.
[6] J. Ding, P. Colegrove, F. Martina, S. Williams, R. Wiktorowicz, M.R. Palt, Development of a laminar flow local shielding device for wire + arc additive manufacture, J. Mater. Process. Technol. 226 (2015) 99–105.
[7] S. Simhambhatla, K. Karunakaran, U. Chandrasekhar, M. Somashekara, A study of the mechanical properties of objects built through weld-deposition, Proc. Inst. Mech. Eng. Part B 227 (no. 8) (2013) 1138–1147.
[8] P.A. Colegrove, H.E. Coules, J. Fairman, F. Martina, T. Kashoob, H. Mamash, L.D. Cozzolino, Microstructure and residual stress improvement in wire and arc additively manufactured parts through high-pressure rolling, J. Mater. Process. Technol. 213 (10) (2013) 1782–1791.
[9] J. Ding, P. Colegrove, J. Mehnen, S. Ganguly, P. Almeida Sequeira, F. Wang, S. Williams, Thermo-mechanical analysis of Wire and Arc Additive Layer Manufacturing process on large multi-layer parts, Comput. Mater. Sci 50 (12) (2011) 3315–3322.
[10] N. Murugan, R.S. Parmar, Stainless steel cladding deposited by automatic gas metal arc welding, Weld. J. 76 (no. 10) (1997), pp. 391. s-403 s.
[11] G.C. Anzalone, C. Zhang, B. Wijnen, P.G. Sanders, J.M. Pearce, A low-cost open-source metal 3-D printer, IEEE Access 1 (2013) 803–810.
[12] B. Krick, J. Vail, B. Persson, W. Sawyer, Optical in situ micro tribometer for analysis of real contact area for contact mechanics, adhesion, and sliding experiments, Tribol. Lett. 45 (2012) 185–194.
[13] G.M. Erickson, M.A. Sidebottom, J.F. Curry, D.I. Kay, S. Kuhn-Hendricks, M.A. Norell, W.G. Sawyer, B.A. Krick, Paleo-tribology: development of wear measurement techniques and a three-dimensional model revealing how grinding dentitions self-wear to enable functionality, Surf. Topogr. Metrol. Prop. 4 (no. 2) (2016) 1–12.
[14] M.D. Abramoff, P.J. Magalhaes, S.J. Ram, Image processing with ImageJ, Biophoton. Int. 11 (7) (2004) 36–42.
[15] D.G. Harlow, M.Z. Wang, R.P. Wei, Statistical analysis of constituent particles in 7075-T6 aluminum alloy, Metall. Mater. Trans. 37A (2006) 3367–3373.
[16] P.J. Diggle, Statistical Analysis of Spatial Point Patterns, Academic Press, New York, 1983.
[17] X.Y. Wang, D.Y. Li, Mechanical, electrochemical and tribological properties of nano-crystalline surface of 304 stainless steel, Wear 12 (2003) 836–845.
[18] E. Arbtin, G. Murphy, Correlation of Bickers Hardness Number, Modulus of Elasticity, and the Yield Strength for Ductile Metals, United States Atomic Energy Commmission, Ames, Iowa, 1953.
[19] L.S.Z.Z. Zhang P, General relationship between strength and hardness, Mater. Sci. Eng. A 529 (2011) 62–73.
[20] C.M. Young, B. Walser, E.P. Abrahamson, O.D. Sherby, Elimination of yield point phenomenon in mild steel by warm working, Scr. Metall. 9 (1) (1975) 35–38.